Monthly Notices of the ROYAL ASTRONOMICAL SOCIETY

MNRAS **496,** 5528–5551 (2020) doi:10.1093/mnras/staa1903
Advance Access publication 2020 July 7

Magnetic fields in the formation of the first stars – I. Theory versus simulation

Christopher F. McKee [1,2]★ Athena Stacy[2] and Pak Shing Li[2]

[1]*Department of Physics, University of California, Berkeley, CA 94720, USA*
[2]*Department of Astronomy, University of California, Berkeley, CA 94720, USA*

Accepted 2020 June 26. Received 2020 June 24; in original form 2020 March 12

ABSTRACT

While magnetic fields are important in contemporary star formation, their role in primordial star formation is unknown. Magnetic fields of the order of 10^{-16} G are produced by the Biermann battery due to the curved shocks and turbulence associated with the infall of gas into the dark matter minihaloes that are the sites of formation of the first stars. These fields are rapidly amplified by a small-scale dynamo until they saturate at or near equipartition with the turbulence in the central region of the gas. Analytical results are given for the outcome of the dynamo, including the effect of compression in the collapsing gas. The mass-to-flux ratio in this gas is two to three times the critical value, comparable to that in contemporary star formation. Predictions of the outcomes of simulations using smooth particle hydrodynamics (SPH) and grid-based adaptive mesh refinement are given. Because the numerical viscosity and resistivity for the standard resolution of 64 cells per Jeans length are several orders of magnitude greater than the physical values, dynamically significant magnetic fields affect a much smaller fraction of the mass in simulations than in reality. An appendix gives an analytical treatment of free-fall collapse, including that in a constant-density background. Another appendix presents a new method of estimating the numerical viscosity; results are given for both SPH and grid-based codes.

Key words: methods: numerical – stars: formation – ISM: magnetic fields – dark ages, reionization, first stars.

1 INTRODUCTION

The first stars and galaxies were the early drivers of cosmic evolution, directing the Universe towards the highly structured state we observe today. The radiation emitted during the lifetime of the first stars (also known as primordial, Population III, or Pop III stars), and the metals they released through supernova (SN) explosions and stellar winds, left a crucial imprint on their environment. In the wake of Pop III stars, the first galaxies emerged to continue the process of reionizing the Universe (e.g. Kitayama et al. 2004; Sokasian et al. 2004; Whalen, Abel & Norman 2004; Alvarez, Bromm & Shapiro 2006; Johnson, Greif & Bromm 2007) and chemically enriching the intergalactic medium (IGM; e.g. Madau, Ferrara & Rees 2001; Chen et al. 2017; reviewed in Karlsson, Bromm & Bland-Hawthorn 2013). Before Pop III stars first formed, no metals or dust existed to aid in the cooling and condensation of gas into stars. Primordial star formation was instead driven by cooling through H_2 transitions. Thus, Pop III stars are believed to have initially formed at $z \sim 20$–30 in small dark matter haloes of mass $\sim 10^6$ $M_\odot$, since these 'minihaloes' were the first structures whose constituent gas had a sufficient H_2 abundance to allow for star formation (Haiman, Thoul & Loeb 1996; Tegmark et al. 1997; Yoshida et al. 2003).

Pop III stars are too faint to be detectable by even next-generation telescopes such as the *James Webb Space Telescope* (Gardner et al. 2006). Understanding of these objects must instead come from numerical simulations and indirect observational constraints. Early studies found that Pop III stars are massive and form in isolation (Abel, Bryan & Norman 2002; Bromm, Coppi & Larson 2002; Bromm & Loeb 2004; Yoshida, Omukai & Hernquist 2008). More recent work has modified this picture (Turk, Abel & O'Shea 2009; Stacy, Greif & Bromm 2010, 2012; Bromm 2013; Stacy, Bromm, & Lee 2016): While the Pop III initial mass function (IMF) is top-heavy, improved simulations have found that a given massive Pop III star forms within a disc and tends to have a number of companions with a range of masses ($\sim$1 to several tens of $M_\odot$; e.g. Clark, Glover & Klessen 2008; Clark et al. 2011).

These studies did not include magnetic fields, although magnetic fields have significant effects in contemporary star formation (see the reviews by McKee & Ostriker 2007 and Krumholz & Federrath 2019). Magnetic fields have existed on a wide range of astronomical scales for most of the history of the Universe (see Beck et al. 1996; Kulsrud & Zweibel 2008; Durrer & Neronov 2013; Subramanian 2016 for reviews). In describing the strength of primordial fields, we sometimes use the comoving field, $B_c = a^2 B$, where $a = 1/(1 + z)$ is the cosmological scale factor; this is the value the field would have if it evolved from redshift z to today under the conditions of flux freezing. Primordial magnetic fields could have arisen during inflation, but such fields are extremely small unless the conformal invariance of the electromagnetic field is broken (Turner & Widrow 1988). Even in that case, the fields produced are on very small scales and will dissipate unless turbulent motions stretch and fold the field, thereby generating a small-scale dynamo that amplifies the field (Durrer & Neronov 2013). For example, turbulence driven by primordial density fluctuations drives a small-scale dynamo acting on inflation-generated seed fields that Wagstaff et al. (2014)

★ E-mail: cmckee@astro.berkeley.edu

estimate produces fields of maximum strength $B_c \sim 10^{-15}$ G on comoving scales of ∼0.1 pc (under the assumption that they were in equipartition with the turbulence when they were created). Magnetic fields can also be produced during an electroweak or QCD phase transition, although in the standard model these transitions are not first order and do not result in observable fields today (Durrer & Neronov 2013). If effects beyond the standard model render one or both these transitions to be first-order phase transitions, then they could result in fields of 10^{-15} to 10^{-12} G on scales of 0.1–100 pc today (Wagstaff et al. 2014). In any case, it is believed that the peak in the field strength occurs on a scale $L \sim v_A/H$, where L is the correlation length of the field, H is the Hubble parameter, and v_A is the Alfvén velocity; the comoving field decreases, and the comoving correlation length increases, with cosmic time, and are now related by $B_c \sim 10^{-14} L_c/(1\ \mathrm{pc})$ G (Banerjee & Jedamzik 2004). This is only slightly above the observed lower limit on the intergalactic magnetic field of a few times 10^{-15} G for correlation lengths of 1 pc based on gamma-ray observations of blazars (Neronov & Vovk 2010; Taylor, Vovk & Neronov 2011), although this method of inferring the field has recently been called into question (Broderick et al. 2018; Alves Batista, Saveliev & de Gouveia Dalpino 2019). A more exotic possibility is that the field results from the chiral magnetic effect in the epoch of the electroweak transition due to a difference in the number of left- and right-handed fermions, which Schober et al. (2018) estimate could give a field of $B_c \sim 2 \times 10^{-16} (L_c/1\ \mathrm{pc})^{-1/2}$ G. In sum, inflation or phase transitions in the early Universe could generate intergalactic fields as large as $\sim 10^{-13}$ G on scales of ∼10 pc (Durrer & Neronov 2013); however, these estimates rest on an uncertain theoretical foundation.

Weaker magnetic fields can definitely be produced through the Biermann battery process, in which non-parallel gradients in the electron density and pressure generate solenoidal electric fields that in turn generate magnetic fields (Biermann 1950; Biermann & Schlüter 1951). For the Galaxy, these authors estimated that this process would produce a field of the order of 10^{-19} G and that this field would be subsequently amplified in a turbulent dynamo until it reached approximate equipartition with the turbulent motions. Since the turbulent velocity increases with scale, the magnetic field will also increase. Research since then has filled in this basic picture (Pudritz & Silk 1989; Kulsrud et al. 1997; Davies & Widrow 2000; Xu et al. 2008). Fields created during galaxy formation can be produced in oblique shocks, with an estimated strength of $\sim 10^{-18}$ to 10^{-19} G (Pudritz & Silk 1989; Xu et al. 2008). Weaker fields ($\sim 10^{-24.5}$ G at redshifts $z \sim$ 10–100) can form throughout the Universe after recombination due to misalignment of the density gradients in the gas and the temperature gradients in the cosmic background radiation (Naoz & Narayan 2013).

The small-scale dynamo is also active during the initial collapse of the turbulent gas in cosmic minihaloes that leads to the formation of the first stars. Numerical simulations have shown that the field grows due to both a small-scale dynamo and compression; a resolution of at least 32–64 cells per Jeans length is required to see the operation of the dynamo (Sur et al. 2010; Federrath et al. 2011b; Turk et al. 2012). These authors noted that the growth rate of the field increases with the Reynolds number and therefore with resolution; the results were far from converged even at a resolution of 128 cells per Jeans length. A subsequent simulation (Koh & Wise 2016), which focused on the evolution of the star, its H II region, and the subsequent SN, found considerably less dynamo amplification. None of these simulations were carried to the point that the field reached approximate equipartition with the turbulent motions prior to the formation of the star. In view of the challenges faced by numerical simulations, semi-analytical approaches have been used to follow the evolution of the field until it saturates: Schleicher et al. (2010) developed a simple model for the turbulence in a collapsing cloud and the growth of the field, and both they and Schober et al. (2012b) used the Kazantsev (1968) equation to follow the growth of the field in a turbulent medium. A comprehensive analytical treatment of the small-scale dynamo under conditions appropriate for the formation of the first stars and galaxies has been given by Xu & Lazarian (2016).

Magnetic fields can be amplified at later evolutionary times also. A dynamo driven in a primordial protostellar disc can amplify the field to the point that the magneto-rotational instability can operate in the disc, and it can also lead to the generation of outflows and jets (Tan & Blackman 2004). Simulations by Machida et al. (2006) found that protostellar jets would be launched for initial field strengths of $B > 10^{-9} \left(n/10^3\ \mathrm{cm}^{-3}\right)^{2/3}$ G. The simulations of Machida & Doi (2013), which resolved the gas collapse up to protostellar density and the subsequent evolution for the next few hundred years, found that sufficiently strong magnetic fields ($>10^{-9}$ G in a Bonnor–Ebert sphere with a central density of 10^4 cm^{-3}) prevented disc formation and led to the formation of a single massive star. However, they did not include the turbulence that has been found to be important in the formation of magnetized discs (Gray, McKee & Klein 2018), and their assumption of a uniform initial field is incompatible with having a field of that magnitude being produced by a small-scale dynamo.

Peters et al. (2014) studied the influence of both magnetic fields and metallicity on primordial gas cut out from cosmologically simulated minihaloes, testing metallicities ranging from $Z = 0$ to $10^{-4}\,Z_\odot$ and initial magnetic fields ranging from 0 to 10^{-2} G. They followed their simulations until 3.75 $M_\odot$ of gas was converted into star(s), and similarly find multiple sink formation in all cases except for metal-free gas with the largest initial magnetic fields. Sharda, Federrath & Krumholz (2020) carried out a large number of simulations of primordial star formation with different initial field strengths and found that the magnetic field strongly suppressed fragmentation, thereby significantly reducing the number of low-mass stars that could survive until today. Both groups conclude that magnetic fields are essential to determining the IMF as well as the binarity and multiplicity of Pop III stars.

This is the first of two papers in which we study the magnitude of the magnetic fields expected in the formation of the first stars and the effects of these fields on the formation of these stars. As described earlier, the fields generated either in the early Universe or by the Biermann battery after recombination are very weak, so the fields must be amplified in a small-scale dynamo by a large factor in order to have an effect on star formation. In this first paper, we review the theory of such dynamos for both the case in which the dissipation is due to resistivity, which is relevant for numerical simulations, and the case in which the dissipation is due to ambipolar diffusion, which is relevant for star formation in the epoch between recombination and reionization (Section 2). We assume that the initial conditions for the dynamos are set by the Biermann battery operating in the gas that falls into a dark matter minihalo. We evaluate the quantities that govern the behaviour of the dynamos (Table 1) and then include the effects of gravitational collapse in our analysis. In Section 3, we apply these results to the formation of the first stars and show that magnetic fields can grow to approximate equipartition in the gravitational collapse that forms these stars. It is not currently possible to carry out simulations with the resolution needed to accurately represent

Table 1. Turbulent, ambipolar diffusion-dominated dynamo in weakly ionized plasma in a cosmic minihalo.

Parameter	Equation	Evaluation[a]
$\epsilon = \frac{v_\ell^3}{\ell} \rightarrow \frac{v^3(r)}{r}$	–	$3.20\times10^{-6}\left(\frac{v_{\rm t,5}^3}{r_2}\right)$ cm^2 s^{-3}
$\ell_\nu = \left(\frac{\nu^3}{\epsilon}\right)^{1/4}$	(3)	$1.42\times10^{16}\left(\frac{T_3^{0.63}r_2^{1/4}}{v_{\rm t,5}^{3/4}n_{\rm H}^{3/4}}\right)$ cm
$v_\nu = (\epsilon\nu)^{1/4}$	(3)	$3.59\times10^{3}\left(\frac{T_3^{0.21}v_{\rm t,5}^{3/4}}{r_2^{1/4}n_{\rm H}^{1/4}}\right)$ cm s^{-1}
$\Gamma_\nu = \frac{v_\nu}{\ell_\nu} = \left(\frac{\epsilon}{\nu}\right)^{1/2}$	(3)	$2.52\times10^{-13}\left(\frac{v_{\rm t,5}^{3/2}n_{\rm H}^{1/2}}{T_3^{0.42}r_2^{1/2}}\right)$ s^{-1}
$B_\nu = (4\pi\rho_\nu)^{1/2}v_\nu$	(12)	$1.90\times10^{-8}\left(\frac{v_{\rm t,5}^{3/4}T_3^{0.21}n_{\rm H,\,\nu}^{1/4}}{r_2^{1/4}}\right)$ G
$B_{\rm eq} = (4\pi\rho_{\rm eq})^{1/2}v_{\rm t}$	(18)	$5.30\times10^{-7}\,v_{\rm t,5}n_{\rm H,\,eq,i}^{1/2}$ G
$t_{\rm nl} = \frac{8}{3\Gamma_\nu}\ln\left[\left(\frac{\rho_0}{\rho_\nu}\right)^{2/3}\frac{B_\nu}{B_0}\right]^b$	(13)	$3.35\times10^{5}\left(\frac{T_3^{0.42}r_2^{1/2}}{v_{\rm t,5}^{3/2}n_{\rm H,\,\nu}^{1/2}}\right)\ln\left[\left(\frac{n_{\rm H,0}}{n_{\rm H,\,\nu}}\right)^{2/3}\frac{B_\nu}{B_0}\right]$ yr
$P_{\rm m} = \frac{\nu}{\eta_{\rm AD}} = \frac{R_{\rm m}}{Re}$	(1)	$1.29\left(\frac{\phi_{\rm d}x_{\rm i,-4}T_3^{0.80}r_2^{1/2}n_{\rm H}^{1/2}}{v_{\rm t,5}^{3/2}}\right)\left(\frac{B_\nu^2}{B^2}\right)$
$\mathcal{R} = \frac{6\nu_{\rm ni}}{\Gamma_\nu} = 6\left(\frac{B^2}{B_\nu^2}\right)P_{\rm m}$	(28)	$7.72\left(\frac{\phi_{\rm d}x_{\rm i,-4}T_3^{0.80}r_2^{1/2}n_{\rm H}^{1/2}}{v_{\rm t,5}^{3/2}}\right)$
$Re = \frac{Lv_L}{\nu} \rightarrow \frac{rv(r)}{\nu}$	(4)	$6.04\times10^{5}\left(\frac{v_{\rm t,5}r_2n_{\rm H}}{T_3^{0.84}}\right)$
$R_{\rm m} = \frac{Lv_L}{\eta_{\rm AD}} \rightarrow \frac{rv(r)}{\eta_{\rm AD}}$	(4)	$1.00\times10^{3}\left(\frac{\phi_{\rm d}x_{\rm i,-4}T_3^{0.38}r_2n_{\rm H}}{v_{\rm t,5}}\right)\left(\frac{B_{\rm eq}^2}{B^2}\right)$

[a] r_2 is the outer scale of the turbulence in units of 10^2 pc, $v_{\rm t,5}$ is the turbulent velocity on that scale in units of 10^5 cm s^{-1}, $n_{\rm H}$ is the density of hydrogen in cm^{-3}, $T_3 = T/(10^3\ {\rm K})$, $x_{\rm i,-4} = x_{\rm i}/10^{-4}$ is the normalized ionization fraction, and ρ_ν and $\rho_{\rm eq}$ are the densities at $B = B_\nu$ (equation 60) and $B_{\rm eq}$ (equation 69), respectively. $\phi_{\rm d}$ (equation A14) measures the importance of the ion–neutral drift velocity; $\phi_{\rm d} = 1$ for $v_{\rm d} = 0$ and $\phi_{\rm d} \propto (v_{\rm d}/c_{\rm s})^{3/4}$ for highly supersonic drift. We assume $n_{\rm He}/n_{\rm H} = 1/12$ so that $\mu_{\rm H} \equiv \rho/n_{\rm H} = 1.33m_{\rm H}$.
[b] Assumes no dissipation and that $P_{\rm m} \gtrsim 1$ for Ohmic resistivity and $\mathcal{R} \gtrsim 1$ if the resistivity is due to ambipolar diffusion.

the viscosity and resistivity of the gas that forms the first stars, so in Section 4 we estimate the magnitude of the fields that can be produced by either a smooth particle hydrodynamics (SPH) or a grid-based simulation of a small-scale dynamo. Appendix A summarizes the values of the viscosity and the ambipolar and Ohmic resistivities under the conditions appropriate for the formation of the first stars. In Appendix B, we describe gravitational collapse in the presence of a fixed dark matter background. Finally, in Appendix C, we estimate the numerical viscosity for both grid-based and SPH codes, and the resistivity for grid-based codes. In Paper II (Stacy et al., in preparation), we simulate the formation of a first star from cosmological initial conditions and compare the results with the theory developed here.

2 SMALL-SCALE DYNAMOS

As noted in the Introduction, the initial cosmological seed field is very weak, but it can be rapidly amplified by the small-scale dynamo driven by turbulence (Batchelor 1950; Kazantsev 1968; Kulsrud & Anderson 1992; Schekochihin et al. 2002a; Schekochihin, Boldyrev & Kulsrud 2002b; Schleicher et al. 2010; Schober et al. 2012a; Xu & Lazarian 2016). Direct experimental evidence for dynamo amplification of magnetic fields in a laser-produced turbulent plasma has been obtained by Tzeferacos et al. (2018). The behaviour of the dynamo is set by the relative sizes of the viscous scale, ℓ_ν, where ν is the kinematic viscosity, and the magnetic dissipation scale, ℓ_η, where η is the resistivity (Kulsrud & Anderson 1992; Schober et al. 2012b). In a fully ionized plasma, ℓ_η is set by Ohmic resistivity, but in a partially ionized plasma it is generally set by ambipolar diffusion.[1] The ratio of these scales is determined by the magnetic Prandtl number

$$P_{\rm m} \equiv \frac{\nu}{\eta}. \tag{1}$$

For Kolmogorov turbulence, $\ell_\nu/\ell_\eta = P_{\rm m}^{1/2}$ for $P_{\rm m} \gg 1$ (Schekochihin et al. 2002b) and $\ell_\nu/\ell_\eta = P_{\rm m}^{3/4}$ for $P_{\rm m} \ll 1$ (Moffatt 1961). Most dilute astrophysical plasmas are highly conducting and have $P_{\rm m} \gg 1$ (e.g. Schekochihin et al. 2002b), so that the resistive scale is small compared to the viscous scale. Turbulence both stretches and folds the field. The stretching occurs on the eddy scale, and for $P_{\rm m} \gg 1$ the fastest eddies are on the viscous scale. The eddy motions result in many field reversals, which can survive down to the magnetic dissipation scale. As a result, the field becomes very anisotropic, varying on a scale $\ell_\nu \gg \ell_\eta$ parallel to the field and on a scale that decreases in time from ℓ_ν to a scale $\geq\ell_\eta$ normal to the field. In the

[1] The ambipolar resistivity as defined by Pinto, Galli & Bacciotti (2008) is sometimes termed the magnetic diffusivity.

opposite limit in which $P_{\rm m} \ll 1$, the field cannot respond to eddies at the viscous scale, but is instead driven by eddies on the resistive scale. In either case, the dynamo is termed 'small-scale', since the field is amplified on scales smaller than the outer scale of the turbulence.

Since primordial gas cannot cool to very low temperatures, the turbulence in regions where the first stars form is generally transonic or subsonic, so for simplicity we shall assume Kolmogorov turbulence in our analytical discussion. The turbulent velocity on a scale ℓ in the inertial range therefore satisfies $v_\ell \propto \ell^{1/3}$. The quantity v_ℓ^3/ℓ is then constant in the inertial range and is comparable to the specific energy dissipation rate, ϵ. Following Pope (2000), we define the velocity on the scale ℓ as

$$v_\ell \equiv (\epsilon \ell)^{1/3}. \tag{2}$$

One can show that then $(1/2)v_\ell^2 \simeq kE(k)$, where $E(k)\mathrm{d}k$ is the energy in the range of wavenumbers $\mathrm{d}k$. In particular, $v_\nu = (\epsilon \ell_\nu)^{1/3}$ is the velocity that eddies at the viscous scale, ℓ_ν, would have in the absence of dissipation at that scale. The viscous scale length, ℓ_ν, is defined by the condition that the Reynolds number at the scale ℓ_ν is unity, $Re(\ell_\nu) = \ell_\nu v_\nu/\nu = 1$, so that $\nu = \ell_\nu v_\nu$. As a result, we have

$$\ell_\nu = \left(\frac{\nu^3}{\epsilon}\right)^{1/4}, \quad v_\nu = (\epsilon\nu)^{1/4}, \quad \Gamma_\nu = \frac{v_\nu}{\ell_\nu} = \left(\frac{\epsilon}{\nu}\right)^{1/2}, \tag{3}$$

where Γ_ν is the characteristic eddy turnover rate on the viscous scale. The hydrodynamic and magnetic Reynolds numbers of a turbulent flow, Re and $R_{\rm m}$, depend on the outer scale of the turbulence, L:

$$Re \equiv \frac{Lv_L}{\nu} = \left(\frac{L}{\ell_\nu}\right)^{4/3} = \left(\frac{v_L}{v_\nu}\right)^4, \quad R_{\rm m} \equiv \frac{Lv_L}{\eta} = P_{\rm m} Re. \tag{4}$$

2.1 Ideal MHD

If the resistivity is negligible, so that $P_{\rm m} \gg 1$, and if the fluid is incompressible, then in the kinematic limit the equation for the magnetic energy density per unit mass, $\mathcal{E}_B = B^2/(8\pi\rho) = (1/2)v_{\rm A}^2$, where $v_{\rm A}$ is the Alfvén velocity, is (Batchelor 1950; Kulsrud & Anderson 1992)

$$\frac{\mathrm{d}\mathcal{E}_B}{\mathrm{d}t} = 2\Gamma\mathcal{E}_B, \tag{5}$$

where, as noted earlier, the growth rate, Γ, is dominated by eddies on the viscous scale,

$$\Gamma = \frac{\langle \boldsymbol{BB} : \boldsymbol{\nabla v}\rangle}{\langle B^2\rangle} \simeq \frac{v_\nu}{\ell_\nu} \equiv \Gamma_\nu, \tag{6}$$

and where the angular brackets $\langle\,\rangle$ represent a volume average (Schekochihin et al. 2002a). Now, in Kolmogorov turbulence, the eddy turnover rate at the viscous scale is related to that at the outer scale by

$$\frac{v_\nu}{\ell_\nu} = \frac{1}{\ell_\nu}\left(\frac{v_L \ell_\nu^{1/3}}{L^{1/3}}\right) = \left(\frac{v_L}{L}\right) Re^{1/2}, \tag{7}$$

where the second step follows from equation (4). Schober et al. (2012a) used the WKB approximation to solve the equation that Kazantsev (1968) derived to describe the kinematic dynamo in incompressible, turbulent fluids and showed that when the resistivity is negligible ($P_{\rm m} \gg 1$), the growth rate of the field is

$$\Gamma = \frac{37}{36}\left(\frac{v_L}{L}\right) Re^{1/2} = \frac{37}{36}\left(\frac{v_\nu}{\ell_\nu}\right) \simeq \Gamma_\nu. \tag{8}$$

In other words, the growth rate is the eddy turnover time at the viscous scale in this limit. Hence, in the kinematic limit the field energy grows as

$$\mathcal{E}_B = \mathcal{E}_{B0}\, \mathrm{e}^{2\Gamma_\nu t}. \tag{9}$$

On scales larger than the peak of the magnetic power spectrum, the magnetic power spectrum is given by

$$M(k,t) = M_0 (k\ell_\nu)^{3/2} \exp\left(\frac{3}{4}\int \Gamma_\nu\, \mathrm{d}t\right) \tag{10}$$

(Kazantsev 1968; Kulsrud & Anderson 1992; Schekochihin et al. 2002a; Xu & Lazarian 2016),[2] where we have adopted the normalization of Xu & Lazarian (2016). Under the assumptions that the spectrum varies as $k^{3/2}$ up to the wavenumber at the peak, $k_{\rm p}$, and then cuts off rapidly (Kulsrud & Anderson 1992; Xu & Lazarian 2016) and that the magnetic energy is initially concentrated at the viscous scale, $k_{\rm p}\ell_\nu \sim 1$, the energy in the field is

$$\mathcal{E}_B(t) = \frac{1}{2}\int_0^{k_p} M(k,t)\mathrm{d}k = \mathcal{E}_{B0}(k_{\rm p}\ell_\nu)^{5/2} \exp\left(\frac{3}{4}\int \Gamma_\nu\, \mathrm{d}t\right), \tag{11}$$

where $\mathcal{E}_{B0} = M_0/(5\ell_\nu)$ and we have set $\Gamma = \Gamma_\nu$, as is appropriate for $P_{\rm m} > 1$. Our normalization for $\mathcal{E}_B$ differs by a factor of 5 from that adopted by Xu & Lazarian (2016); it gives $\mathcal{E}_{B0} = \mathcal{E}_B(t=0)$ at $t = 0$ for $k_{\rm p}(t=0) = \ell_\nu^{-1}$. This relation is valid so long as the dynamo is in the kinematic stage and is driven by eddies at the viscous scale, even in the presence of dissipation, since the exponential growth occurs on large scales where dissipation is negligible. In the initial stage of the dynamo, when dissipation is negligible on all relevant scales, the field energy exponentiates as $\exp(2\Gamma_\nu t)$ (equation 9). It follows from equation (11) that if the spectrum cuts off sharply for $k > k_{\rm p}$ in this case, then $k_{\rm p} \propto \exp[(1/2)\Gamma_\nu t]$. (In fact, the spectrum does not cut off sharply at $k_{\rm p}$ and the actual peak of the power spectrum evolves as $\exp[(3/5)\Gamma_\nu t]$; Schekochihin et al. 2002a.) As noted earlier, in the absence of dissipation the field energy is concentrated at a wavenumber $k_{\rm p}$ that becomes increasingly larger than the viscous scale ℓ_ν^{-1} with time as the eddies wind up the field.

The subsequent evolution of the field has been discussed by Schober et al. (2015), who considered a range of turbulent Mach numbers such that $v_\ell \propto \ell^\theta$ with $1/3 \le \theta \le 1/2$, and by Xu & Lazarian (2016), who focused on the case of subsonic turbulence ($\theta = 1/3$) and obtained good agreement with simulations; we shall follow the latter treatment here. Xu & Lazarian (2016) pointed out that the exponential amplification slows when the field energy first reaches equipartition with the viscous eddies on the scale ℓ_ν, so that $\mathcal{E}_B = (1/2)v_\nu^2 \equiv E_\nu$. The corresponding equipartition field (with $v_{\rm A}^2 = v_\nu^2$) is

$$B_\nu = (4\pi\rho)^{1/2} v_\nu = (4\pi\rho)^{1/2}(\epsilon\nu)^{1/4} \tag{12}$$

from equation (3). In the subsequent transition stage, the turbulent cascade maintains the viscous-scale eddies while at the same time amplifying the field on successively larger scales until the peak in the magnetic power spectrum reaches ℓ_ν^{-1}. They assume that the energy at the peak (equation 11) remains equal to E_ν during this evolution. The transition stage ends when $k_{\rm p}\ell_\nu = 1$, so that the magnetic forces can stop the eddies at that scale.

At this time ($t = t_{\rm nl}$), the dynamo enters the fully non-linear stage. Setting $\mathcal{E}_B(t_{\rm nl}) = E_\nu = B_\nu^2/(8\pi\rho)$ for $k_{\rm p}\ell_\nu = 1$ in equation (11) gives

$$t_{\rm nl} = \frac{4}{3\Gamma_\nu}\ln\left(\frac{E_\nu}{\mathcal{E}_{B0}}\right) = \frac{8}{3\Gamma_\nu}\ln\left(\frac{B_\nu}{B_0}\right) \quad (P_{\rm m} \gg 1) \tag{13}$$

[2]Kazantsev (1968) actually gave a range of exponents for the wavenumber; Kulsrud & Anderson (1992) appear to have been the first to specify that the exponent is 3/2.

for the time at which the dynamo enters the fully non-linear stage. For example, if the equipartition field at the viscous scale is 10 orders of magnitude above the initial field, then this time is $t_{\rm nl} = 61\,\ell_\nu/v_\nu = (3760/Re)^{1/2} L/v_L$. Subsequently, it is the smallest eddies that are not suppressed by magnetic forces that dominate the magnetic energy, so that $\mathcal{E}_B \simeq (1/2)v_\ell^2$ and $\Gamma = \chi v_\ell/\ell$, where χ is of order unity. It follows that

$$\frac{{\rm d}\mathcal{E}_B}{{\rm d}t} = 2\left(\frac{\chi v_\ell}{\ell}\right)\cdot\frac{1}{2}v_\ell^2 = \chi\epsilon \tag{14}$$

from equation (5) (Schekochihin et al. 2002a). As a result, the magnetic energy in the non-linear stage is

$$\mathcal{E}_B = \mathcal{E}_B(t_{\rm nl}) + \chi\epsilon(t - t_{\rm nl}) \qquad (t > t_{\rm nl}). \tag{15}$$

Kulsrud & Anderson (1992) presented analytical arguments suggesting $\chi = 3/38 = 0.079$ for the case in which the dissipation is dominated by reconnection, and Xu & Lazarian (2016) confirmed this. Note that in these theories the value of χ is independent of the rate of reconnection: Kulsrud & Anderson (1992) assumed Petschek reconnection, which has a rate that depends on $R_{\rm m}$, whereas Xu & Lazarian (2016) assumed turbulent reconnection, which is maximally efficient and has a rate that is independent of $R_{\rm m}$. Numerical simulations confirm that χ is significantly smaller than unity: Cho et al. (2009) found $\chi \simeq 0.07$ and Beresnyak (2012) found $\chi \simeq 0.05$. Collectively, these results indicate that

$$\chi^{-1} = 16 \pm 0.1 \text{ dex}, \tag{16}$$

so we shall adopt $\chi = 1/16$ for numerical estimates. For $t \gg t_{\rm nl}$, the time to reach equipartition at a scale ℓ (i.e. the time at which $\mathcal{E}_B = (1/2)v_\ell^2$) is proportional to the eddy turnover time,

$$t_{\rm eq}(\ell) = \frac{(1/2)v_\ell^2}{\chi\epsilon} = \frac{\ell}{2\chi v_\ell}, \tag{17}$$

so that it takes $(2\chi)^{-1} \sim 8$ eddy turnover times at a scale ℓ for the field to reach equipartition at that scale.

The field stops growing when it reaches equipartition with the largest eddies, $B \simeq B_{\rm eq}$, where

$$B_{\rm eq} = (4\pi\rho)^{1/2} v_L = Re^{1/4}\, B_\nu \tag{18}$$

from equations (4) and (12). Simulations suggest that for subsonic solenoidal turbulence the magnetic field saturates at a value $B_{\rm sat} = \phi_{\rm sat} B_{\rm eq}$ with $\phi_{\rm sat} \simeq (3/7)^{1/2} = 0.65$ (Haugen, Brandenburg & Dobler 2004) $\simeq 0.7$ (Federrath et al. 2011a; Brandenburg 2014); for supersonic solenoidal turbulence, Federrath et al.'s (2011a) results imply $\phi_{\rm sat} \simeq 0.14$.

To determine how long it takes for the field to reach equipartition at the scale L, we can use equations (3), (12), and (13) and the fact that $\mathcal{E}_B(t_{\rm nl}) = B_\nu^2/(8\pi\rho)$ to rewrite equation (15) as

$$B^2 = B_\nu^2\left\{1 + 2\chi\left[\Gamma_\nu t - \frac{8}{3}\ln\left(\frac{B_\nu}{B_0}\right)\right]\right\} \qquad (t > t_{\rm nl}). \tag{19}$$

Equation (18) then implies that

$$\Gamma_\nu t_{\rm eq}(L) = \frac{8}{3}\ln\left(\frac{B_\nu}{B_0}\right) + \frac{Re^{1/2} - 1}{2\chi} \simeq 8Re^{1/2}, \tag{20}$$

where the final step is for a large Reynolds number and $\chi = 1/16$. If the field saturates at a value less than $B_{\rm eq}$, the factor $Re^{1/2}$ should be multiplied by $\phi_{\rm sat}^2$.

There is an aspect of this analysis that is overly idealized: We have assumed that the turbulence is established instantaneously, whereas in fact it takes at least an eddy turnover time for the turbulence to develop (e.g. Banerjee & Jedamzik 2004). For a flow that is initialized at some point in time (e.g. at the epoch of recombination), the size of the largest eddy in a turbulent cascade at a time t later is $L \sim v_L t$. As a result, $\epsilon \sim v_L^2/t$, and equation (15) implies

$$\frac{v_{\rm A}^2}{v_L^2} \sim 2\chi\left(1 - \frac{t_{\rm nl}}{t}\right), \tag{21}$$

provided $\mathcal{E}_B(t_{\rm nl})$ is negligible compared to $\mathcal{E}_B(t)$. Since $\chi \simeq 1/16$, it follows that the field will be close to equipartition for $t \gg t_{\rm nl}$, but can never reach it unless there is a boundary that sets a limit on L, as we implicitly assumed in equation (20).

2.2 Evolution of the field in the presence of Ohmic resistivity

The evolution of the field in the presence of Ohmic resistivity, in both the kinematic and non-linear phases, has been worked out by Xu & Lazarian (2016), and we summarize their results in Fig. 1. The magnetic specific energy, $\mathcal{E}_B$, increases monotonically with time, whereas the wavenumber at the peak of the magnetic power spectrum, $k_{\rm p}$, initially increases with time for $P_{\rm m} > 1$; in the non-linear stage, $k_{\rm p}$ decreases with time for all $P_{\rm m}$. Resistivity has no effect on the dynamo if it is sufficiently small, it affects the later part of the kinematic stage of the dynamo for intermediate values of $P_{\rm m}$, and it delays the onset of the non-linear stage of the dynamo for $P_{\rm m} < 1$. The change in the evolution that is apparent in Fig. 1 as one moves from top to bottom is due to the resistive scale, ℓ_η, which is represented by the rightmost vertical line, moving from right to left as $P_{\rm m}$ decreases. The resistive scale is too small to matter in the top panel, and the dynamo evolves as described earlier for ideal MHD. For intermediate values of $P_{\rm m}$ (the middle panel), resistivity prevents the peak wavenumber from growing past the inverse of the resistive scale, ℓ_η^{-1}. When the peak wavenumber is fixed due to resistive dissipation, the growth of the specific magnetic energy becomes

$$\mathcal{E}_B = \mathcal{E}_{B0} P_{\rm m}^{5/4} \exp\left(\frac{3}{4}\int \Gamma_\nu\,{\rm d}t\right) \qquad \left[1 < P_{\rm m} < (E_\nu/\mathcal{E}_{B0})^{1/2}\right] \tag{22}$$

(Xu & Lazarian 2016; see equation 11). Finally, for $P_{\rm m} < 1$ (the bottom panel), the peak in the energy spectrum remains at ℓ_η^{-1} in the kinematic stage. Since $\ell_\eta > \ell_\nu$, the damping scale is in the turbulent cascade, and the eddy turnover rate at the dissipation scale is given by equation (3) with ν replaced by η (e.g. Xu & Lazarian 2016),

$$\Gamma_\eta = \left(\frac{\epsilon}{\eta}\right)^{1/2} = P_{\rm m}^{1/2}\Gamma_\nu. \tag{23}$$

The value of the field energy is given by equation (11) with ν replaced by η and $k_{\rm p}\ell_\eta = 1$,

$$\mathcal{E}_B = \mathcal{E}_{B0}\exp\left(\frac{3}{4}\int \Gamma_\eta\,{\rm d}t\right) \qquad (P_{\rm m} < 1). \tag{24}$$

The condition for the dynamo to enter the non-linear stage is that the field energy equal the kinetic energy of the eddies driving the dynamo. For $P_{\rm m} > 1$, these eddies are at the viscous scale, and the dynamo enters the non-linear stage at the time given in equation (13). For $P_{\rm m} < 1$, so that $\ell_\eta > \ell_\nu$, these eddies are at the resistive scale, and the dynamo enters the non-linear stage at the time given by equation (13) with Γ_ν replaced by Γ_η and B_ν replaced by $B_\eta = P_{\rm m}^{1/4} B_\nu$ (Xu & Lazarian 2016).

In Paper II, we address the evolution of the magnetic field with an SPH code (GADGET-2) that can follow the evolution of the kinematic dynamo and a grid-based code (ORION2) that has full ideal MHD. Neither treats ambipolar diffusion; both have numerical resistivity. Lesaffre & Balbus (2007) have argued that grid-based codes have a numerical magnetic Prandtl number, $P_{\rm m,num}$, between 1 and 2,

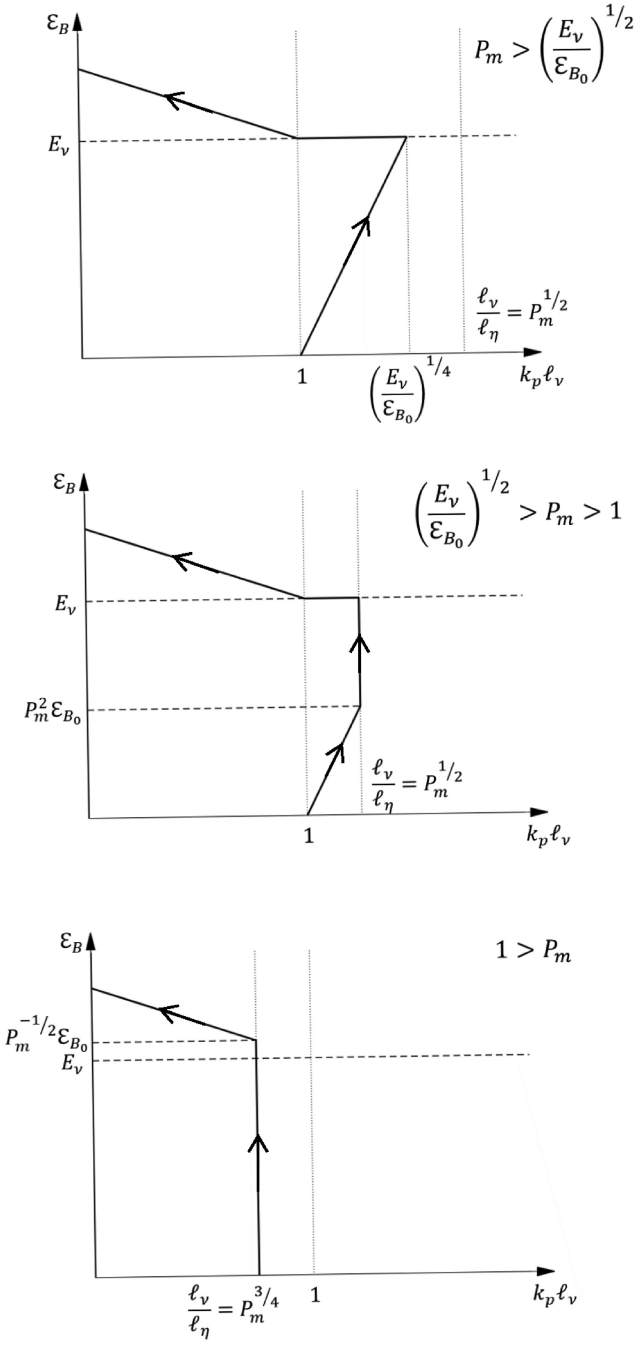

Figure 1. Graphical representation of the theory of Xu & Lazarian (2016) for dynamos with Ohmic resistivity. The magnetic specific energy, $\mathcal{E}_B$, which increases as the dynamo operates, is plotted against the wavenumber at which the magnetic power spectrum peaks, k_p, normalized by the viscous length scale, ℓ_ν. Arrows indicate the direction of time. For very large values of the magnetic Prandtl number, P_m (top panel), k_p increases until the magnetic energy reaches equipartition with the viscous-scale eddies ($\mathcal{E}_B = E_\nu$); $\mathcal{E}_B$ then remains approximately constant as the energy moves to larger scales. Once the peak wavenumber reaches the viscous scale, the energy resumes its growth as it taps the energy of larger eddies. For intermediate P_m (middle panel), the increase in k_p in the kinematic stage stops when k_p reaches the resistive scale. For $P_\mathrm{m} < 1$ (bottom panel), the peak wavenumber is capped at $k_\mathrm{p}\ell_\eta \sim 1$, and non-linear growth does not begin until the field reaches equipartition with the turbulence at that scale.

depending on wavenumber. In Appendix C, we analyse the results of Federrath et al. (2011b) and conclude that $P_\mathrm{m,num} \simeq 1.4$ for grid-based codes, in good agreement with the result of Lesaffre & Balbus (2007). We adopt the same value of $P_\mathrm{m,num}$ for SPH codes.

In order for the dynamo to operate, it is necessary for the magnetic Reynolds number to exceed a critical value, $R_\mathrm{m,cr}$. Using numerical simulations, Haugen et al. (2004) found

$$R_\mathrm{m,cr} \simeq 2\pi \times 35 P_\mathrm{m}^{-1/2} = 220 P_\mathrm{m}^{-1/2} \quad (0.1 \lesssim P_\mathrm{m} \lesssim 3), \tag{25}$$

where the factor 2π has been inserted in order to convert the expression for the Reynolds number used by Haugen et al. (2004), $R_\mathrm{m} = v/(k_\mathrm{f}\eta)$, where $k_\mathrm{f} = 2\pi/L$ is the forcing wavenumber, to the expression adopted here, $R_\mathrm{m} = vL/\eta$. Haugen et al. (2004) found that $R_\mathrm{m,cr}$ begins to increase with P_m somewhere beyond $P_\mathrm{m} = 3$, reaching 220 at $P_\mathrm{m} = 10$. Schober et al. (2012a) solved the Kazantsev equation in the WKB approximation and found $R_\mathrm{m,cr} \simeq 107$ for $P_\mathrm{m} \gg 1$. For supersonic turbulence, Federrath et al. (2014) found $R_\mathrm{m,cr} \simeq 129$, based on large part on simulations with $P_\mathrm{m} = 10$. Since simulations of the formation of the first stars are characterized by transonic turbulence and modest values of P_m, the results of Haugen et al. (2004) are most relevant for our problem, and we shall adopt the value of $R_\mathrm{m,cr}$ in equation (25) here.

2.3 Evolution of the field in the presence of ambipolar diffusion

The first stars form in a weakly ionized plasma in which the dominant resistivity is ambipolar diffusion (Kulsrud & Anderson 1992; Schober et al. 2012b; Xu & Lazarian 2016). For the case of weak ionization ($\rho_\mathrm{i} \ll \rho_\mathrm{n} \simeq \rho$), where ρ_n and ρ_i are the neutral and ion mass densities, the resistivity due to ambipolar diffusion is (e.g. Pinto et al. 2008)

$$\eta_\mathrm{AD} = \frac{B^2}{4\pi\gamma_\mathrm{AD}\rho_\mathrm{i}\rho_\mathrm{n}} = \frac{v_\mathrm{A}^2}{\gamma_\mathrm{AD}\rho_\mathrm{i}} = \frac{v_\mathrm{A}^2}{\nu_\mathrm{ni}}, \tag{26}$$

where γ_AD is the collisional drag coefficient and ν_ni is the neutral–ion collision frequency (see Appendix A). It follows that $\eta_\mathrm{AD} \propto v_\mathrm{A}^2 \propto B^2$, so that the magnetic Prandtl number, $P_\mathrm{m} = \nu/\eta$, starts off very large when evaluated for the primordial field, but then decreases exponentially in time as the small-scale dynamo amplifies the field. The damping rate of magnetic fluctuations due to ambipolar diffusion is (Kulsrud & Anderson 1992)

$$\omega_\mathrm{d} = \frac{1}{3}\frac{k^2\mathcal{E}_B}{\nu_\mathrm{ni}}, \tag{27}$$

where the factor 1/3 comes from averaging the rate over angle.

The growth of the magnetic field in the presence of ambipolar diffusion has been analysed by Kulsrud & Anderson (1992) and, in more detail, by Xu & Lazarian (2016); we follow the latter treatment here (see Fig. 2, which summarizes their results). The first, dissipation-free stage of the kinematic dynamo has been described in Section 2.1. Damping is important at the wavenumber, k_d, at which the damping rate equals the rate at which the field is being stretched, $\omega_\mathrm{d}(k_\mathrm{d}) = \Gamma_\nu$, where it has been assumed that the field is weak enough that $k_\mathrm{d}\ell_\nu > 1$ so that the driving is at the viscous scale. As a result, equation (27) implies

$$k_\mathrm{d}\ell_\nu = \left(\frac{3\nu_\mathrm{ni}\ell_\nu^2\Gamma_\nu}{\mathcal{E}_B}\right)^{1/2} = \left(\frac{\mathcal{R}E_\nu}{\mathcal{E}_B}\right)^{1/2}, \tag{28}$$

where the parameter

$$\mathcal{R} \equiv \frac{6\nu_\mathrm{ni}}{\Gamma_\nu} \tag{29}$$

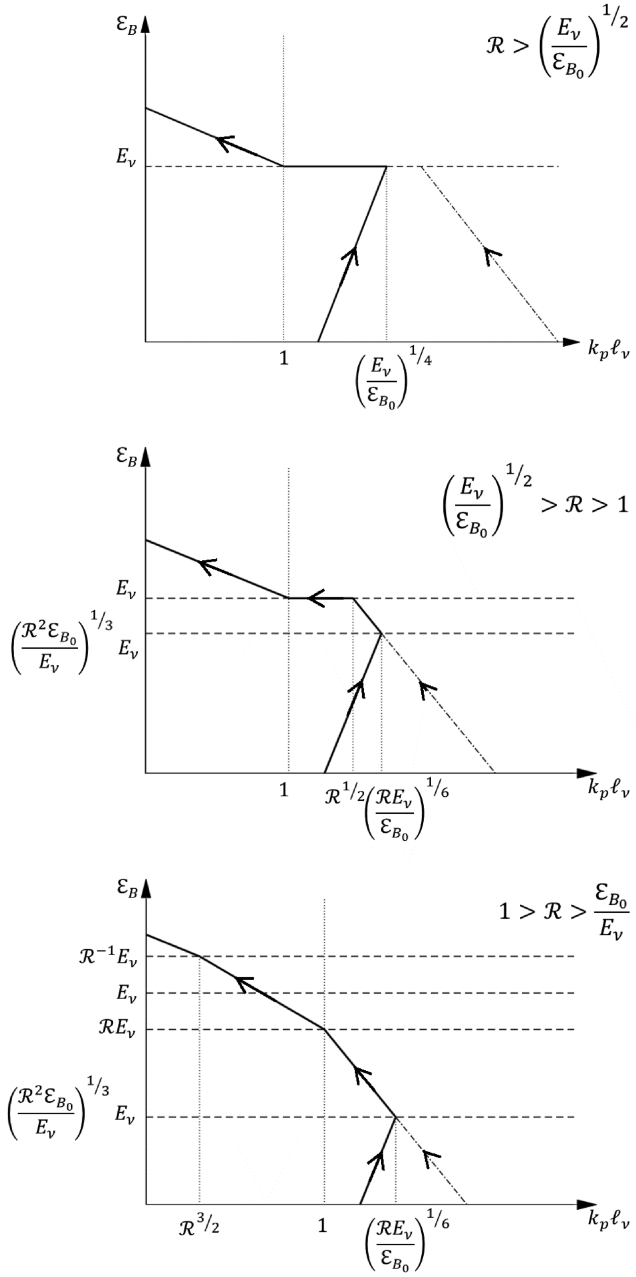

Figure 2. Graphical representation of the theory of Xu & Lazarian (2016) for dynamos in the presence of ambipolar diffusion. The magnetic specific energy, $\mathcal{E}_B$, which increases as the dynamo operates, is plotted against the wavenumber at which the magnetic power spectrum peaks, k_p, normalized by the viscous length scale, ℓ_ν. The zero is suppressed: $\mathcal{E}_B$ begins at $\mathcal{E}_{B0}$ for $k_\mathrm{p}\ell_\nu = 1$. The damping wavenumber, k_d (equation 28, dot–dashed line), decreases as the magnetic energy increases. Arrows indicate the direction of time. For large values of the dynamo ionization parameter, $\mathcal{R}$ (equation 29; top panel), k_p increases until the magnetic energy reaches equipartition with the viscous-scale eddies ($\mathcal{E}_B = E_\nu$). For intermediate $\mathcal{R}$ (middle panel), the damping scale k_d^{-1} becomes large enough that it determines k_p in the later parts of the kinematic stage. For $\mathcal{R} < 1$ (bottom panel), the damping is strong enough that the magnetic specific energy is less than that of the viscous eddies ($\mathcal{E}_B = \mathcal{R}E_\nu < E_\nu$) when the damping scale grows to the viscous scale. Thereafter, $\mathcal{E}_B$ grows as t^2 until the field reaches equipartition with the eddies at k_p, when $\mathcal{E}_B = \mathcal{R}^{-1}E_\nu$. In each case, the leftmost stage of evolution is the same as that for Ohmic resistivity.

plays a role for the case of ambipolar diffusion similar to that P_m plays in the resistive case. Since $\mathcal{R} \propto \nu_\mathrm{ni}$, it varies linearly with the degree of ionization; we therefore term it the 'dynamo ionization parameter'. We can relate it to the magnetic Prandtl number as follows: Since $\eta_\mathrm{AD} \propto v_\mathrm{A}^2 \propto B^2$, we have $P_\mathrm{m} \propto B^{-2}$. For $B = B_\nu$ – i.e. when the field energy is in equipartition with the viscous-scale eddies – we have $v_\mathrm{A}^2 = v_\nu^2$ so that

$$P_\mathrm{m}(B_\nu) = \frac{\nu}{\eta_\mathrm{AD}(B_\nu)} = \frac{\nu}{v_\nu^2/\nu_\mathrm{ni}} = \frac{\nu_\mathrm{ni}}{\Gamma_\nu} = \frac{1}{6}\mathcal{R}. \tag{30}$$

Hence, $\mathcal{R}$ is a measure of the magnetic Prandtl number when $B = B_\nu$. If $\mathcal{R}$ is not too large ($\mathcal{R} \lesssim (E_\nu/\mathcal{E}_{B0})^{1/2}$), the kinematic dynamo enters a dissipative stage of evolution in which the peak of the magnetic energy spectrum is at the damping wavenumber, $k_\mathrm{p} = k_\mathrm{d}$, and one finds from equations (11) and (28) that the magnetic energy grows as $\mathcal{E}_B \propto \exp(\Gamma_\nu t/3)$. If $\mathcal{R} > 1$ (middle panel of Fig. 2), equation (28) shows that $k_\mathrm{p} = k_\mathrm{d}$ exceeds ℓ_ν^{-1} when equipartition is reached at ℓ_ν^{-1} (i.e. when $\mathcal{E}_B = E_\nu$). As in the ideal case, the system then undergoes a transitional stage in which k_p drops to ℓ_ν^{-1} while $\mathcal{E}_B = E_\nu$. The transitional stage ends and the non-linear stage begins at t_nl given by equation (13). On the other hand, for $\mathcal{R} < 1$ (bottom panel of Fig. 2), the first dissipative stage ends when k_d drops to ℓ_ν^{-1}, which occurs prior to equipartition according to equation (28). Xu & Lazarian (2016) showed and Xu et al. (2019) confirmed computationally that subsequently the magnetic energy grows as $\mathcal{E}_B \propto t^2$ for a time interval

$$\Delta t_\mathrm{damp} = \frac{23}{3\Gamma_\nu}\left(\frac{1}{\mathcal{R}} - 1\right), \tag{31}$$

so that the dynamo enters the fully non-linear stage at a time $t_\mathrm{nl} + \Delta t_\mathrm{damp}$, where t_nl is given in equation (13). As in the case of Ohmic resistivity, transition from the case of very high $\mathcal{R}$ in the top panel of Fig. 2 to low $\mathcal{R}$ in the bottom panel can be visualized as the effects of the line representing $\mathcal{E}_B(k_\mathrm{d})$, no longer vertical, sweeping from right to left as $\mathcal{R}$ decreases.

To gain more insight into the different stages of the dynamo, one can evaluate the magnetic Reynolds number at the dynamo driving scale, ℓ_dr. With the aid of equation (26), we obtain

$$R_\mathrm{m}(\ell_\mathrm{dr}) = \frac{\mathcal{R}}{6}\left(\frac{\Gamma_\nu}{v_\mathrm{dr}/\ell_\mathrm{dr}}\right)\frac{v_\mathrm{dr}^2}{v_\mathrm{A}^2}. \tag{32}$$

If the driving is at the viscous scale ($\ell_\mathrm{dr} = \ell_\nu$), we have $v_\mathrm{dr}/\ell_\mathrm{dr} = \Gamma_\nu$ so that $R_\mathrm{m}(\ell_\mathrm{dr}) > (1/6)\mathcal{R}$ in the kinematic stage ($v_\mathrm{A}^2 < v_\mathrm{dr}^2$). For $\mathcal{R} \geq 1$, the dynamo enters the non-linear stage at $R_\mathrm{m}(\ell_\nu) = (1/6)\mathcal{R}$. For $\mathcal{R} < 1$, one can use the results of Xu & Lazarian (2016) to show that $R_\mathrm{m} = 1/6$ in the damping stage.

We summarize the parameters describing the growth of the magnetic field when ambipolar diffusion dominates in Table 1. The values of the viscosity, ν, and the ambipolar resistivity, η_AD, are given in Appendix A. Before applying the results in this table, we first consider the origin of the field and the effect of a time-dependent background on the dynamo.

2.4 The Biermann battery in a turbulent medium

As shown by Biermann (1950) (see also Biermann & Schlüter 1951), magnetic fields can be generated in an accelerating plasma, a mechanism referred to as the 'Biermann battery'. An electric field arises in such a plasma in order to maintain charge neutrality if the force per unit mass on the electrons differs from that on the ions. If the velocity field has a curl, so will the electric field, which produces a magnetic field by Faraday's law. These authors estimated

the magnetic field by noting that the electric field is of the order of $E \sim (m_{\rm H}/e){\rm d}v/{\rm d}t \sim (m_{\rm H}/e)v^2/\ell$, so that $\partial B/\partial t \sim cE/\ell \sim (cm_{\rm H}/e)v^2/\ell^2$ and $B \sim (cm_{\rm H}/e)v/\ell = 1.0 \times 10^{-4}(v/\ell)$. As noted in the Introduction, they estimated that this process would produce a field of the order of 10^{-19} G in a galaxy.

Harrison (1969, 1970) gave a more rigorous derivation of this result for the case in which the force is radiation drag on the electrons, and Kulsrud et al. (1997) did so for the case in which the force is due to a pressure gradient. The latter authors pointed out that the equation for the vorticity and that for the magnetic field have the same form,

$$\frac{\partial \boldsymbol{\omega}}{\partial t} - \boldsymbol{\nabla}\times(\boldsymbol{v}\times\boldsymbol{\omega}) = \frac{\boldsymbol{\nabla}\rho\times\boldsymbol{\nabla}p}{\rho^2} + \nu\nabla^2\boldsymbol{\omega}, \tag{33}$$

$$\frac{\partial \boldsymbol{B}}{\partial t} - \boldsymbol{\nabla}\times(\boldsymbol{v}\times\boldsymbol{B}) = -\frac{m_{\rm a}c}{e(1+x_i)}\left(\frac{\boldsymbol{\nabla}\rho\times\boldsymbol{\nabla}p}{\rho^2}\right) + \eta\nabla^2\boldsymbol{B}, \tag{34}$$

where $m_{\rm a} = \rho/n_{\rm a}$ is the mean mass of the atoms (both neutral and ionized), $n_{\rm a}$ is the number density of atoms, and $x_i \equiv n_{\rm e}/n_{\rm a}$ is the ionization fraction. These equations are based on the assumption that x_i, ν, and η are constant. The source for $\boldsymbol{\omega}$ and $\boldsymbol{B}$ is the baroclinic term due to non-parallel density and pressure gradients ($\boldsymbol{\nabla}\rho\times\boldsymbol{\nabla}p \neq 0$), which arise naturally in curved shocks.

Kulsrud et al. (1997) stated that the viscous and resistive terms in equations (33) and (34) can be ignored in determining the post-shock vorticity. To see this for the viscous term, for example, go into the shock frame, so that $\partial/\partial t = 0$, and integrate equation (33) across the shock front. Writing $p = \rho c_{\rm s}^2$, where $c_{\rm s}$ is the isothermal sound speed, we find

$$\Delta(v\omega) \sim \frac{\Delta\left(c_{\rm s}^2\ln\rho\right)}{L} + \nu\Delta(\boldsymbol{\nabla}\omega), \tag{35}$$

where we have assumed that the vectors in equation (33) are not nearly parallel and where L is the scale of the curvature of the shock. The post-shock sound speed is of the order of the shock velocity, $v_{\rm s}$, so the first term on the right-hand side is of the order of $v_{\rm s}^2/L$. The vorticity generated by the shock is of the order of $v_{\rm s}/L$. The turbulent cascade behind the shock begins on the scale L, so the vorticity changes on that scale just behind the shock; as a result, the second term is of the order of $\nu v_{\rm s}/L^2$. It follows that the ratio of the first term to the second is of the order of $v_{\rm s}L/\nu = Re \gg 1$, so the viscous term does not affect the generation of vorticity in the shock. A similar argument can be made for the evolution of the magnetic field provided that the shock is collisional, as it should be at low velocities in a primarily neutral medium.

It follows that if the vorticity and field are initially zero, they will grow in tandem; for the case in which the force is a pressure gradient, the field is

$$\boldsymbol{B} = -\left[\frac{m_{\rm a}c}{(1+x_i)e}\right]\boldsymbol{\omega}. \tag{36}$$

If the force is due to radiation drag on the electrons, the field is $\boldsymbol{B} = -(m_{\rm a}c/e)\boldsymbol{\omega}$ in a fully ionized plasma (Harrison 1969); if the plasma is partially ionized, one can show that the field is larger by a factor of x_i^{-1}. Balbus (1993) showed that fields generated by the Biermann battery are so weak that the Larmor radius, $r_{\rm L,i} = v_{\rm ion}/\Omega_{\rm i} \simeq (v_{\rm ion}/v_\ell)\ell$, can exceed the scale ℓ on which the vorticity is measured; here, $v_{\rm ion}$ is the velocity of an individual ion, whereas v_ℓ is the mean velocity on the scale ℓ and is less than $v_{\rm ion}$ for subsonic flows.

Numerically, for a vorticity $\omega = v_{\rm t}(r)/r$ and for $n_{\rm He} = n_{\rm H}/12$, this field is

$$B = 1.29 \times 10^{-4}\omega = 4.17 \times 10^{-19}\left(\frac{v_{\rm t,5}}{r_2}\right)\ {\rm G}, \tag{37}$$

where $v_{\rm t,5}$ is the turbulent velocity in units of 10^5 cm s^{-1} and r_2 is the radius in units of 100 pc. Although very weak fields ($\sim 10^{-24.5}$ G) can be generated within linear perturbations in the post-recombination Universe (Naoz & Narayan 2013), significantly stronger fields are generated in curved shocks associated with galaxy formation (Pudritz & Silk 1989) and the accretion of gas into minihaloes.

Turbulence leads to an increase in the field in two separate stages, the turbulent Biermann battery and then the small-scale dynamo. First, since the post-shock flow is at high Re (Table 1), the vorticity on a scale L leads to a turbulent cascade in which the vorticity increases in time as it cascades to smaller and smaller scales, $\omega \sim v_\ell/\ell \simeq (L/\ell)^{2/3}v_L/L$. Correspondingly, the magnetic field increases on smaller scales according to equation (36) (Kulsrud 2005). For $P_{\rm m} > 1$, this process ceases when viscous damping terminates the turbulent cascade on the scale ℓ_ν. The vorticity on this scale is $\sim\Gamma_\nu$, so that the field due to a turbulent Biermann battery is

$$B = 3.24 \times 10^{-17}\left(\frac{v_{\rm t,5}^{3/2}n_{\rm H}^{1/2}}{T_3^{0.42}r_2^{1/2}}\right)\ {\rm G} \tag{38}$$

at the end of this process (see Table 1).

Once the turbulent cascade has been established, in a time of the order of L/v_L, the vorticity no longer grows and the growth of the field is due to a small-scale dynamo as discussed earlier. Here, the difference between equations (33) and (34) becomes important: $\boldsymbol{\omega} = \boldsymbol{\nabla}\times\boldsymbol{v}$ is a function of $\boldsymbol{v}$, whereas $\boldsymbol{B}$ is not. Thus, while the vorticity no longer grows once the turbulent cascade is established, the magnetic field can grow exponentially.

2.5 Dynamos in a time-dependent background

To this point, we have assumed that the dynamo is operating in a medium with a density that is independent of time. However, the gas that forms a primordial star first expands with the cosmological expansion, contracts with the formation of a minihalo, and then contracts further as it forms a protostellar core. As a result, the evolution equations for the small-scale dynamo must be revised to account for the temporal evolution of the mean density. For homologous expansion or collapse, mass and flux conservation imply that $\rho \propto 1/r^3$ and $B \propto 1/r^2$, where r is the distance from an arbitrary point in a homologous expansion or from the centre of the collapse, which is assumed to be spherical. As a result, $B \propto \rho^{2/3}$. Collapse is generally not homologous, so these relations need not hold locally. Nonetheless, prior to the formation of a star, the mean density and mean field satisfy $\bar{B} \propto \bar{\rho}^{2/3}$ under the conditions of flux freezing. Lazarian et al. (2015) and references therein argue that reconnection in a turbulent medium leads to violations of flux freezing, and Li, McKee & Klein (2015) found evidence for this in their simulations. Those same simulations found that this was a modest effect, however, and were consistent with an overall dependence $\mathcal{E}_B \propto B^2/\rho \propto (\rho/\rho_0)^{1/3} = \xi^{1/3}$. Following Schleicher et al. (2010) and Schober et al. (2012b), we assume that the effects of the dynamo and the time-dependent background are separable. As a result, equations (11) and (24) for the kinematic dynamo become

$$\mathcal{E}_B = \mathcal{E}_{B0}\xi^{1/3}(k_{\rm p}\ell_\nu)^{5/2}\exp\left(\frac{3}{4}\int\Gamma_\nu\,{\rm d}t\right) \quad (P_{\rm m} > 1), \tag{39}$$

$$\mathcal{E}_B = \mathcal{E}_{B0}\xi^{1/3}\exp\left(\frac{3}{4}\int\Gamma_\eta\,{\rm d}t\right) \quad (P_{\rm m} < 1), \tag{40}$$

where

$$\xi \equiv \frac{\rho}{\rho_0} \tag{41}$$

is the compression ratio and ρ_0 is the initial density. After a star forms, these equations need not hold, since the mean gas density no longer varies as $1/r^3$ and the magnetic flux released from the star can evolve in a complex manner.

Recall that the dynamo enters the non-linear stage when $\mathcal{E}_B = E_\nu$, the specific energy of the viscous-scale eddies, and also that $k_{\rm p}\ell_\nu = 1$ at this time. (If ambipolar diffusion dominates, the case in which $\mathcal{R} < 1$ is more complicated as discussed in Section 2.3, so we do not discuss that case in this section.) Let ρ_ν be the density at the time that the dynamo enters the non-linear stage, and let $\langle\Gamma_\nu\rangle$ be the time-averaged value of Γ_ν prior to that time. Expressing $\mathcal{E}_B$ in terms of B, we then find that the dynamo enters the non-linear stage at

$$t_{\rm nl} \simeq \frac{8}{3\langle\Gamma_\nu\rangle} \ln\left(\xi_\nu^{-2/3}\,\frac{B_\nu}{B_0}\right), \tag{42}$$

where $\xi_\nu \equiv \rho_\nu/\rho_0$. As we shall see in Section 3, $t_{\rm nl}$ is expected to be small compared to the dynamical time in the formation of the first stars, so the factor ξ_ν in equation (42) is close to unity and $\langle\Gamma_\nu\rangle \simeq \Gamma_{\nu 0}$, the initial value of Γ_ν. However, this is not the case for the simulations (Section 4).

For the non-linear dynamo ($t > t_{\rm nl}$), equation (14) becomes

$$\frac{{\rm d}\mathcal{E}_B}{{\rm d}t} = \chi\epsilon + \mathcal{E}_B\,\frac{{\rm d}\ln\xi^{1/3}}{{\rm d}t}, \tag{43}$$

where we have assumed that the field has not reached equipartition with motions on the outer scale of the turbulence ($B < B_{\rm eq}$). The scale of the dynamo enters through $\epsilon = v_t^3/\ell$. Equation (43) then gives

$$\mathcal{E}_B(t) = \left(\frac{\xi}{\xi_\nu}\right)^{1/3}\mathcal{E}_{B_\nu} + \chi\xi^{1/3}\int_{t_{\rm nl}}^{t}\epsilon(t')\xi(t')^{-1/3}\,{\rm d}t', \tag{44}$$

where $\mathcal{E}_{B_\nu} = \mathcal{E}_B(t_{\rm nl})$ is given by

$$\mathcal{E}_{B_\nu} \equiv \frac{B_\nu^2}{8\pi\rho_\nu} = \frac{1}{2}v_\nu^2 = \frac{1}{2}(\epsilon\nu)^{1/2} = \frac{1}{2}\,\frac{\epsilon}{\Gamma_\nu}. \tag{45}$$

The first term in equation (44) represents the compression (assuming the density is increasing) of the field at the beginning of the non-linear stage (B_ν), whereas the second term represents the field produced by the non-linear dynamo, including the amplification of that field due to compression.

We approximate the density dependence of a quantity x as $x \propto \rho^{q_x} \propto \xi^{q_x}$. In particular, $\epsilon \propto \rho^{q_\epsilon}$ and $\Gamma \propto \rho^{q_\Gamma}$, so that

$$\mathcal{E}_B(t) = \frac{1}{2}\left(\frac{\xi}{\xi_\nu}\right)^{1/3}\frac{\epsilon_0}{\Gamma_{\nu 0}}\,\xi_\nu^{q_\epsilon - q_\Gamma} + \phi_{\rm ff}\chi\epsilon_0 t_{\rm ff,0}\xi^{1/3}I_{q_\epsilon - 1/3}(\xi_\nu,\xi), \tag{46}$$

where $\xi_\nu = \xi(t_{\rm nl})$, $\Gamma_{\nu 0}$ is evaluated at the initial density, ρ_0, and

$$I_q(\xi_1,\xi_2) \equiv \frac{1}{\phi_{\rm ff}t_{\rm ff,0}}\int_{t(\xi_1)}^{t(\xi_2)}\xi(t')^q\,{\rm d}t' \tag{47}$$

is evaluated in Appendix B, including the effects of dark matter. Here, $t_{\rm ff,0}$ is the free-fall time for the gas alone and $\phi_{\rm ff}$ is a parameter of order unity that allows the collapse time for the gas alone to differ from $t_{\rm ff,0}$ due to the fact that the collapse is not pressureless, for example. Observe that ${\rm d}t \propto {\rm d}t_{\rm ff} \propto {\rm d}\xi/\xi^{3/2}$ so that I_q is a number of order unity for $q < 1/2$ and $\xi \gg 1$.

Define the dynamo amplification factor $\mathcal{A}(t)$ by

$$B(t) \equiv B_0\mathcal{A}(t)\xi^{2/3}; \tag{48}$$

in terms of the specific magnetic energy, this is

$$\mathcal{E}_B = \mathcal{E}_{B0}\mathcal{A}^2(t)\xi^{1/3}. \tag{49}$$

In the kinematic phase, equations (39) and (40) show that $\mathcal{A} = \mathcal{A}_{\rm kin}$ is exponentially sensitive to the input parameters. For the non-linear phase, we have

$$B = B_\nu\mathcal{A}_{\rm nl}(\xi/\xi_\nu)^{2/3} \qquad (\xi > \xi_\nu), \tag{50}$$

where

$$\mathcal{A}_{\rm nl} = \left[1 + 2\phi_{\rm ff}\chi\Gamma_{\nu 0}t_{\rm ff,0}\xi_\nu^{(1/3)+q_\Gamma - q_\epsilon}I_{q_\epsilon - 1/3}(\xi_\nu,\xi)\right]^{1/2} \tag{51}$$

from equation (46) after expressing $\mathcal{E}_B$ in terms of B. Note that the second term is proportional to

$$\Gamma_{\nu 0}t_{\rm ff,0} = \left(\frac{\epsilon_0}{\nu_0}\right)^{1/2}t_{\rm ff,0} = \left(\frac{v_{\rm t}t_{\rm ff,0}}{L_0}\right)Re^{1/2}. \tag{52}$$

For gravitational collapse, the factor in parentheses in the final expression is of order unity, so it follows that $\mathcal{A}_{\rm nl} \propto Re^{1/4}$ for large Re.

We now show that the non-linear dynamo amplifies the field to a significant fraction of equipartition provided the dynamo amplification factor is large ($\mathcal{A}_{\rm nl}^2 \gg 1$). First, consider the case in which the kinematic stage of the dynamo ends early in the collapse, so that $\xi_\nu \sim 1$. Since $\epsilon_0 = v_{\rm t0}^3/L_0$, equation (46) implies

$$\frac{\mathcal{E}_B}{\frac{1}{2}v_{\rm t0}^2} \simeq 2\chi\left(\frac{\phi_{\rm ff}v_{\rm t0}t_{\rm ff,0}}{L_0}\right)\xi^{1/3}I_{q_\epsilon - 1/3}(1,\xi). \tag{53}$$

The factor in parentheses is of order unity; for example, for sonic turbulence in which the outer scale of the turbulence is the Jeans length, $v_{\rm t0}t_{\rm ff,0}/L_0 = (3/32)^{1/2}$. As noted earlier, when $q < 1/2$, corresponding to $q_\epsilon < 5/6$, the factor I_q is a number of order unity for $\xi \gg 1$; on the other hand, for $q \geq 1/2$, I_q is an increasing function of ξ. It follows that even in the absence of the compression factor $\xi^{1/3}$, the non-linear dynamo will bring the field up to an energy of order $2\chi \sim 0.1$ of equipartition. In the opposite case in which the non-linear stage of the dynamo begins late in the collapse ($\xi_\nu \gg 1$), $I_q(\xi_\nu,\xi)$ can be inferred from equation (B17). As a result, the field energy for $\xi \gg \xi_\nu$ is

$$\frac{\mathcal{E}_B}{(1/2)v_{\rm tv}^2} \simeq 2\chi\left(\frac{\phi_{\rm ff}v_{\rm tv}t_{{\rm ff},\nu}}{L_\nu}\right)\frac{2}{3\pi\,((5/6) - q_\epsilon)}\left(\frac{\xi}{\xi_\nu}\right)^{1/3} \tag{54}$$

for $q_\epsilon < 5/6$, where $v_{{\rm t}\nu}$ is the turbulent velocity at a density $\rho(t_{\rm nl}) = \rho(\xi_\nu)$, etc. For $q_\epsilon \geq 5/6$, the field energy is larger than this. Hence, for $\mathcal{A}_{\rm nl}^2 \gg 1$, the non-linear dynamo is efficient at bringing the field close to equipartition when $\xi_\nu \gg 1$ as well. In both cases, the relative importance of amplification of the field by the non-linear dynamo and by compression is given by the ratio $\mathcal{A}_{\rm nl}(\xi_\nu/\xi)^{2/3}$. By contrast, this ratio for the specific magnetic energy, $\mathcal{E}_B$, is $\mathcal{A}_{\rm nl}^2(\xi_\nu/\xi)^{1/3}$, which is generally much larger.

As remarked earlier, Lazarian et al. (2015) have argued that flux freezing is violated due to reconnection in a turbulent medium. We note that the effect of eliminating the effect of compression in the evolution of the non-linear dynamo (i.e. omitting the second term in equation 43) would be to omit the factors of ξ and ξ_ν and replace $q_\epsilon - 1/3$ by q_ϵ in equations (53) and (54); this would not affect the conclusion that the non-linear dynamo is capable of bringing the field close to equipartition in a gravitational collapse.

We now estimate the magnitude of the field in the gas that forms the first stars.

3 PREDICTED MAGNETIC FIELD IN THE FORMATION OF THE FIRST STARS

We first discuss the initial Biermann field expected in a minihalo (or galaxy) and then the final value that results from the turbulent

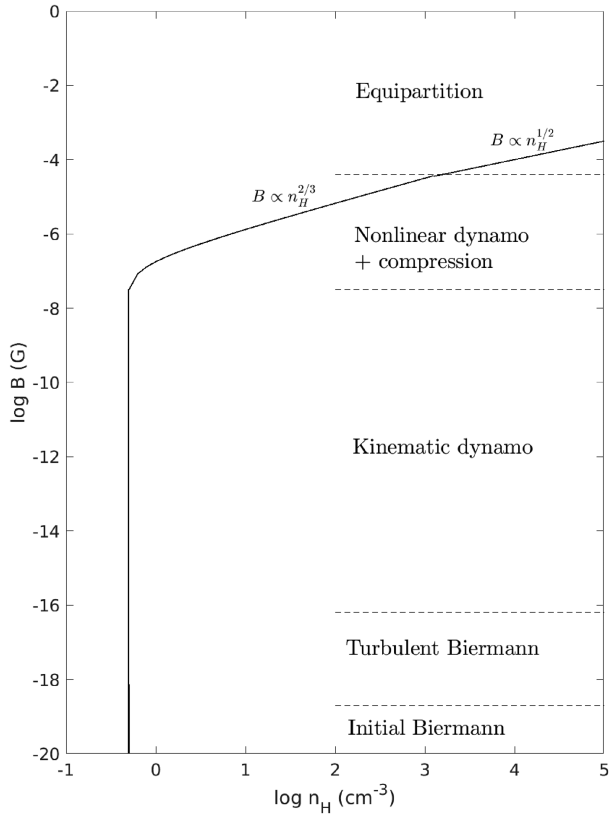

Figure 3. Predicted growth of the magnetic field in a minihalo of total mass $3 \times 10^5\,\mathrm{M}_\odot$ at $z = 25$ under the assumption that the initial field is zero. We have assumed that the turbulent velocity is half the virial velocity ($\phi_t = 0.5$) and that $T = 10^3$ K. The initial Biermann battery due to curved shocks on the scale of the minihalo generates a field of about 2×10^{-19} G. As turbulence cascades to smaller scales, the field generated by the Biermann battery increases to $\sim 10^{-16}$ G. A small-scale dynamo amplifies this field to about 3×10^{-8} G during the kinematic stage. Because the growth rate of the dynamo is so large in this stage, the density is about constant in time. The non-linear dynamo is much slower, so the baryons are compressed by a factor of $\sim$4000 during this stage as they collapse due to the combined gravity of the dark matter and the baryons. In this stage, the field grows to about 5×10^{-5} G. The dynamo amplifies the field by only a factor of $\sim$7 in the non-linear stage; most of the growth of the field is due to compression. The non-linear stage ends when the field reaches equipartition with the turbulence, with $v_t \simeq 2$ km s^{-1}. Subsequently, the field remains in approximate equipartition with the turbulence.

cascade. We show that the Biermann field is amplified rapidly in the kinematic stage of a small-scale dynamo, so that the density in this stage is approximately equal to the initial value. In the non-linear phase of evolution of the dynamo, the field is amplified primarily by the compression due to the gravitational collapse that leads to star formation. This compression drives the field to equipartition, and it remains approximately in equipartition until non-ideal MHD effects take over. An overview of the predicted evolution of the field is shown in Fig. 3.

3.1 The initial field

As discussed in the Introduction, processes in the very early Universe might create comoving fields in the range $B_c \sim 10^{-15}$ to 10^{-12} G, but these processes are hypothetical. The Biermann battery process prior to reionization produces much weaker fields, $B \sim 10^{-25}$ to 10^{-24} G, in the IGM (Naoz & Narayan 2013) or $B \sim 10^{-19}$ G in protogalaxies (Biermann & Schlüter 1951); the comoving fields are smaller by a factor of $a^2 = 1/(1+z)^2$. However, these fields are based on well-established physics, so we focus on them here.

The field produced by the Biermann battery in a minihalo or a galaxy in the process of formation is due to the oblique shocks (Pudritz & Silk 1989) associated with the formation of these objects. As discussed in Section 2.4, the magnitude of this field is $1.29 \times 10^{-4}\omega$, where ω is the vorticity. We estimate the vorticity on the outer scale of the turbulence as $\omega \sim v_{\rm vir}/r_{\rm vir}$, where $r_{\rm vir} = (3M_{\rm m}/4\pi\rho_{\rm mh})^{1/3}$ and $v_{\rm vir} = (GM_{\rm m}/r_{\rm vir})^{1/2}$ are the virial radius and velocity, respectively, where $M_{\rm m}$ is the mass of all the matter in the halo, including the dark matter, and where $\rho_{\rm mh}$ is the average matter density in the minihalo. It follows that

$$\omega \sim \frac{v_{\rm vir}}{r_{\rm vir}} = \left(\frac{4\pi G\rho_{\rm mh}}{3}\right)^{1/2}, \tag{55}$$

where for a simple tophat model of the formation of the minihalo, $\rho_{\rm mh}$ is approximately $18\pi^2$ times the ambient density in the Hubble flow at that time (e.g. Barkana & Loeb 2001),

$$\rho_{\rm mh} = \frac{27\pi H_0^2\Omega_{\rm m}}{4G}\left(\frac{1+z}{26}\right)^3. \tag{56}$$

Here, we have normalized to a redshift of 25, since that is a typical redshift at which a minihalo collapses (Greif et al. 2012; Stacy et al., in preparation). For simplicity, we henceforth make the approximation $1 + z \simeq 26 z_{25}$, where $z_{25} = z/25$, which is accurate to within 1 per cent for $20 < z < 33$ and accurate to 4 per cent for $z > 12$. Following Stacy et al. (in preparation), we set $H_0 = 70$ km s^{-1} Mpc^{-1}, $\Omega_{\rm m} = 0.30$, and $\Omega_{\rm b} = 0.04$. It follows that the matter density in the minihalo is $\rho_{\rm mh} = 8.62 \times 10^{-24} z_{25}^3$ g cm^{-3}, so that $\omega \sim 1.5 \times 10^{-15} z_{25}^{3/2}$ s^{-1} and $B \sim 2.0 \times 10^{-19} z_{25}^{3/2}$ G at the outer scale of the turbulence. At $z \sim 25$, this field is almost exactly as Biermann & Schlüter (1951) estimated.

As discussed in Section 2.4, the turbulent cascade increases the vorticity, and therefore the field, on smaller scales. To evaluate the final Biermann field, which occurs on the viscous scale where the vorticity is a maximum ($\omega \simeq \Gamma_\nu$), and the properties of the subsequent dynamo, we assume that the turbulence is governed by the properties of the minihalo. We then have for the outer scale of the turbulence in the minihalo $r \simeq r_{\rm vir} = 123 M_{\rm m,6}^{1/3}/z_{25}$ pc, where $M_{\rm m,6} = M_{\rm m}/(10^6\,\mathrm{M}_\odot)$ (cf. Barkana & Loeb 2001). The virial velocity is $v_{\rm vir} = 5.9 M_{\rm m,6}^{1/3} z_{25}^{1/2}$ km s^{-1}. Simulations indicate that the turbulent velocity is somewhat less than this; for example, the results of Greif et al. (2012) show that $v_t \simeq 2$ km s^{-1} to within a factor of 1.5 in the range $r \sim$ 5–50 pc for $M_{\rm m} \simeq 3 \times 10^5\,\mathrm{M}_\odot$, corresponding to $v_t \simeq 0.5 v_{\rm vir}$, and a similar result was obtained by Stacy et al. (in preparation). We therefore set

$$v_t = \phi_t v_{\rm vir} \tag{57}$$

and adopt $\phi_t = 0.5$ as a fiducial value. The density of hydrogen in the minihalo corresponding to the matter density $\rho_{\rm mh}$ is $n_{\rm H} = (\Omega_{\rm b}/\Omega_{\rm m})\rho_{\rm mh}/\mu_{\rm H} = 0.52 z_{25}^3$ cm^{-3}, where $\mu_{\rm H} = 2.23 \times 10^{-24}$ g is the mass per H atom. Equation (38) then implies that the final Biermann field is

$$B_0 = 3.0 \times 10^{-16}\left(\frac{\phi_t^{3/2} M_{\rm m,6}^{1/3} z_{25}^{11/4}}{T_3^{0.42}}\right)\ \mathrm{G}. \tag{58}$$

For a minihalo with $M_{\rm m} = 3 \times 10^5\,\mathrm{M}_\odot$ at $z = 25$, this gives $B_0 \simeq 7 \times 10^{-17}$ G (with $\phi_t = 0.5$ and $T_3 = 1$).

3.2 The kinematic dynamo

The field produced by the Biermann battery is too weak to have any dynamical effects, so the dynamo begins in the kinematic, dissipation-free stage and the field exponentiates as $B \propto \exp(\Gamma_\nu t)$ (Section 2.1). In order to determine the subsequent evolution of the field, we must first determine how long the kinematic stage lasts in comparison with the dynamical time of the minihalo. Ambipolar diffusion is the dominant dissipation mechanism for $B \gtrsim 10^{-13} n_{\rm H}$ G (Appendix A3), and as discussed in Section 2.3, the properties of the dynamo in the presence of ambipolar diffusion are governed by dynamo ionization parameter, $\mathcal{R} = 6\nu_{\rm ni}/\Gamma_\nu$ (equation 29). Using the just cited values of the density and radius of the minihalo, we find

$$\mathcal{R} = 1.2 \left[\frac{\phi_{\rm d} x_{\rm i,-4} T_3^{0.80} z_{25}^{1/4}}{(2\phi_{\rm t})^{3/2} M_{\rm m,6}^{1/3}} \right] \tag{59}$$

from Table 1, where $x_{\rm i,-4} = x_{\rm i}/10^{-4}$ is the normalized ionization fraction. The results of Greif et al. (2012) give $x_{\rm i,-4} \sim 1$ for $r \gtrsim 10$ pc. For $T \gtrsim 500$ K, which is generally the case for the average gas in the minihalo (Abel et al. 2002; Greif et al. 2012), this implies $\mathcal{R} \gtrsim 0.7/M_{\rm m,6}^{1/3}$. This is larger than the value found by Xu & Lazarian (2016) since the ion–neutral collision rate in the post-recombination universe is larger than the value they adopted, as discussed in Appendix A. Since $\mathcal{R}$ is of order unity, the evolution of the dynamo is intermediate between the tracks shown in the bottom two parts of Fig. 2, so the scale of the turbulent field in the kinematic stage remains constant at about ℓ_ν. Furthermore, we can use equation (42) for the time at which the dynamo becomes non-linear, $t_{\rm nl}$. Recall that $t_{\rm nl} \propto \ln(B_\nu/(B_0 \xi_\nu^{2/3})$ and that the initial field in the minihalo is $B_0 \simeq 10^{-16}$ G from equation (58). Initially, the dynamics of the gas in the minihalo are determined by the dynamical time, $t_{\rm vir} = r_{\rm vir}/v_{\rm vir} = 20.4 z_{25}^{-3/2}$ Myr. Anticipating that $t_{\rm nl}/t_{\rm vir}$ will be <1, we infer that the density is about constant so that the density at the end of the kinematic stage, ρ_ν, is about the same as the initial density (i.e. $\xi_\nu \simeq 1$) and $\langle \Gamma_\nu \rangle \simeq \Gamma_\nu$. We then obtain

$$B_\nu = 5.80 \times 10^{-8} \phi_{\rm t}^{3/4} T_3^{0.21} z_{25}^{11/8} M_{\rm m,6}^{1/6} \, {\rm G} \tag{60}$$

from Table 1. In evaluating $t_{\rm nl}$, we set $\phi_{\rm t} = 1/2$, and in the logarithmic factor we set the remaining parameters equal to unity, so that

$$\frac{t_{\rm nl}}{t_{\rm vir}} \simeq 0.10 \left(\frac{T_3^{0.42}}{M_{\rm m,6}^{1/3} z_{25}^{5/4}} \right). \tag{61}$$

We conclude that for a typical minihalo, the dynamo can reach a non-linear amplitude in a time significantly less than the virial time.

Reference to Fig. 2 shows that the dissipation-free stage in the kinematic dynamo lasts until $\mathcal{E}_B = (\mathcal{R}^2 \mathcal{E}_{B0}/E_\nu)^{1/3} E_\nu$, which corresponds to a magnetic field $B \simeq (\mathcal{R}^{1/2} B_\nu/B_0)^{2/3} B_0$. For $\mathcal{R}$ and the remaining parameters all of order unity, this implies that the field is amplified by almost factor of 10^6 before dissipation becomes important. Once that occurs, the field grows more slowly, $B \propto \exp(\Gamma_\nu t/6)$ (Kulsrud & Anderson 1992; Xu & Lazarian 2016). For $\mathcal{R} \gtrsim 1$, as is the case here, this exponential growth continues until the dynamo reaches the non-linear stage at $t = t_{\rm nl}$.

3.3 The non-linear dynamo

As noted earlier, the value of the dynamo ionization parameter, $\mathcal{R}$, is initially of order unity. As the gas collapses in the non-linear stage of the dynamo, $\mathcal{R} \propto x_{\rm i} n_{\rm H}^{1/2} r^{1/2}$ from Table 1. Since the gas is in ionization equilibrium, the ionization varies as $n_{\rm H}^{-1/2}$ so that $\mathcal{R} \propto r^{1/2} \propto \xi^{-1/6}$. As we shall see, dynamo amplification in the non-linear stage is significant only during the initial stages of the collapse, so we shall continue to use the results for $\mathcal{R} \gtrsim 1$. The field is then given by equation (50) with $\mathcal{A}_{\rm nl}$ given by equation (51). The non-linear amplification factor $\mathcal{A}_{\rm nl}$ depends on how the energy dissipation rate depends on density, $\epsilon \propto \rho^{q_\epsilon}$, with $q_\epsilon = 3q_\nu - q_L$, through the factor $I_{q_\epsilon - 1/3}(\xi_\nu, \xi)$ (equation 51). Since $t_{\rm nl}$ is only a fraction of the dynamical time, $t_{\rm vir}$, it follows that the density at $t_{\rm nl}$ is close to the initial density, $\rho_\nu \simeq \rho_0$, so that $\xi(t_{\rm nl}) = \xi_\nu \simeq 1$. The maximum value of $I_q(1, \xi)$ is reached when the collapse is complete, and as shown in equation (B18), it is of order unity provided that $q_\epsilon - 1/3 < 1/2$, which it generally is. Simulations such as those of Greif et al. (2012) show that although the turbulent velocity is roughly constant, it does vary by a factor of $\lesssim 3$ in a complex manner, so the effective value of q_ϵ is uncertain. For a simple analytical estimate, we shall take advantage of the fact that $I_{q,\infty} = \mathcal{O}(1)$ and set $q = q_\epsilon - (1/3) = 0$. Equation (47) then gives $I_{0,\infty} = t_{\rm coll}/(\phi_{\rm ff} t_{\rm ff,0})$. Approximating the collapse time as $t_{\rm vir}$ and recalling that $t_{\rm nl} \ll t_{\rm vir}$, we find from equation (51) that the total amplification by the non-linear dynamo is

$$\mathcal{A}_{\rm nl,tot} \sim (1 + 2\chi \Gamma_{\nu 0} t_{\rm vir})^{1/2} . \tag{62}$$

Noting that $t_{\rm vir} = (3/4\pi G \rho_{\rm mh})^{1/2}$, we find

$$\mathcal{A}_{\rm nl,tot} \sim \left[1 + 66 (2\phi_{\rm t})^{3/2} z_{25}^{5/4} T_3^{-0.42} M_{\rm m,6}^{1/3} \right]^{1/2} , \tag{63}$$

so the non-linear dynamo amplifies the field by less than an order of magnitude in a minihalo. This relatively small amplification is because the field energy grows linearly in time in the non-linear dynamo, but the time available for growth varies as $\xi^{-1/2}$ and is small in the late stages of the collapse. Using equations (B5) and (B17), one can show that 90 per cent of the amplification by the dynamo is completed before the time that $\xi = 30$. (The fact that the dynamo amplification is concentrated in the early stages of the collapse justifies our assumption that we can follow the evolution of the non-linear dynamo with the initial value of $\mathcal{R} \propto \xi^{-1/6}$, which is of order unity.) As shown in Fig. 3, the growth of the field is dominated by compression ($B \propto \xi^{2/3} \propto n_{\rm H}^{2/3}$) for most of the non-linear stage.

3.4 Equipartition

As the collapse continues, the field eventually reaches approximate equipartition with the turbulence. When does this occur? We anticipate that it occurs only after significant compression, at a time close to the time $t_{\rm coll}$ at which the gas in the minihalo has collapsed. Now, for $B > B_\nu$ we have

$$\mathcal{E}_B = \mathcal{E}_{B_\nu} \mathcal{A}_{\rm nl}^2 \xi^{1/3} \tag{64}$$

from equation (50) with $\xi_\nu \simeq 1$. With the aid of equations (45) and (3), we have $\mathcal{E}_{B_\nu} \simeq (1/2)(\epsilon_0 \nu_0)^{1/2} = (1/2)\epsilon_0/\Gamma_{\nu 0}$. Since $\mathcal{A}_{\rm nl,tot}^2 \gg 1$ from equation (63), it follows that the first term in equation (62), representing the field due to the kinematic dynamo, is negligible. We then have

$$\mathcal{E}_B \simeq \chi \epsilon_0 \xi^{1/3} t_{\rm vir} \quad (t \simeq t_{\rm coll} \simeq t_{\rm vir}). \tag{65}$$

Since $\epsilon_0 t_{\rm vir} \simeq (v_{\rm t}^3/r_{\rm vir})(r_{\rm vir}/v_{\rm vir})$, this implies that

$$\frac{v_{\rm A}^2}{v_{\rm t}^2} = \frac{\mathcal{E}_B}{(1/2) v_{\rm t}^2} \simeq 2\chi \xi^{1/3} \frac{v_{\rm t}}{v_{\rm vir}} = 2\phi_{\rm t} \chi \xi^{1/3}. \tag{66}$$

Equipartition first occurs when this ratio is unity, corresponding to a compression of

$$\xi_{\rm eq,i} = \frac{1}{(2\phi_{\rm t}\chi)^3} \simeq \frac{4100}{(2\phi_{\rm t})^3}, \tag{67}$$

which is only a small fraction of the total compression the gas experiences as it collapses into a protostar. Note that this condition for equipartition is independent of all the dimensional parameters of the problem, as expected from equations (53) and (54). The corresponding density is

$$n_{\rm H,\,eq,i} = \left(\frac{1}{2\phi_{\rm t}\chi}\right)^3 n_{\rm H,0} \simeq 2.1\times10^3\left(\frac{z_{25}}{2\phi_{\rm t}}\right)^3 {\rm cm}^{-3}. \quad (68)$$

The initial equipartition magnetic field is then

$$B_{\rm eq,i} = \left(4\pi\rho_0 v_{\rm t}^2\right)^{1/2}\xi_{\rm eq,i}^{1/2} \simeq 7.2\times10^{-5}\left[\frac{z_{25}^2 M_{\rm m,6}^{1/3}}{(2\phi_{\rm t})^{1/2}}\right] {\rm G}. \quad (69)$$

As noted by Schleicher et al. (2010), we expect that once the field reaches equipartition, it will remain there as the compression continues, so that the field will increase as $\rho^{1/2}$ (for a constant turbulent velocity) rather than $\rho^{2/3}$ (see Fig. 3). This behaviour is consistent with the results of the simulations of collapsing turbulent cores by Mocz et al. (2017), who found that the field remained close to equipartition with the turbulent energy as the density increased by orders of magnitude. For an initially weak field, they found that the field eventually increased as $\rho^{2/3}$, presumably because the turbulent velocity increased near the nascent protostar; we note that if $v_{\rm t}^2 \propto r^{-1}$, then $B_{\rm eq}^2 \propto \rho/r \propto \rho^{4/3}$. Our conclusion that the dynamo reaches equipartition in the formation of stars at $z \sim 25$ differs from that of Xu & Lazarian (2016), who concluded that equipartition is reached at $t \sim 6\times10^8$ yr (corresponding to $z \sim 8$), because they did not consider the increase in density that accompanies star formation.

As noted in Section 2.1, it is possible that the field could saturate at a value different from the equipartition value,

$$B_{\rm rms}^2 = B_{\rm sat}^2 = 4\pi\phi_{\rm sat}^2\rho v_{\rm t}^2, \quad (70)$$

with $\phi_{\rm sat}$ most likely somewhat less than 1. In that case, the Alfvén Mach number in the saturated state would be $\mathcal{M}_{\rm A} = v_{\rm t}/v_{\rm A} = 1/\phi_{\rm sat}$; the field would be dynamically insignificant for $\phi_{\rm sat} \ll 1$. Equation (66) implies that the field saturates at a compression $\xi_{\rm sat} = \phi_{\rm sat}^6\xi_{\rm eq,i}$. For $\phi_{\rm sat} = 0.7$, corresponding to the subsonic turbulence (e.g. Federrath et al. 2011a) relevant for the formation of the first stars (Abel et al. 2002; Greif et al. 2012), this gives $\xi_{\rm sat} = 480/(2\phi_{\rm t})^3$.

3.5 The magnetic field versus gravity

How does the force associated with the magnetic field compare with that due to gravity? The magnetic critical mass is the mass for which the gravitational and magnetic forces balance. There are two forms for the critical mass, $M_\Phi \simeq \Phi/(2\pi G^{1/2})$, where $\Phi = \pi r^2 B_{\rm rms}$ is the magnetic flux based on the rms field in the cloud, and

$$M_B = \frac{M_\Phi^3}{M^2} = \frac{9}{128\pi^2 G^{3/2}}\left(\frac{{B_{\rm rms}}^2}{\rho^{4/3}}\right)^{3/2}, \quad (71)$$

where $M(r)$ is the gas mass inside r (e.g. McKee & Ostriker 2007). The force of gravity exceeds that due to magnetic fields for $M > M_\Phi$ or $M > M_B$, so a necessary condition for gravitational collapse is that these inequalities be satisfied (note that $M_\Phi = M_B$ for $M = M_\Phi$, so that this is actually a single condition).

As the baryons collapse, they form a core with a power-law density profile, $\rho \propto r^{-k_\rho}$ with $k_\rho \simeq 2.2$. For example, a fit to the results of Greif et al. (2012) and Stacy et al. (in preparation) gives $k_\rho \simeq 2.3$ and 2.16, respectively, while the theoretical model of Tan & McKee (2004) has $k_\rho = 20/9 \simeq 2.22$. The fraction of the mass with a density greater than ρ is then

$$M(>\rho)/M_0 = M(>\xi)/M_0 = \xi^{-(3-k_\rho)/k_\rho}, \quad (72)$$

where M_0 is the total mass of gas in minihalo; for $k_\rho = 2.2$, this is $M(>\xi)/M_0 = \xi^{-0.36}$. The field is at its equipartition value for the inner 5 per cent of the core for $\phi_{\rm t} = 1/2$ since $M(>\xi_{\rm eq})/M_0 = 0.05(2\phi_{\rm t})^{1.08}$. As an example, for a minihalo of mass $3\times10^5\,{\rm M}_\odot$, we have $M_0 = 4\times10^4\,{\rm M}_\odot$, so that the central $2000\,{\rm M}_\odot$ has an equipartition field. If the field saturates at a value other than the equipartition value, then the mass of gas with a saturated field would be $2000\phi_{\rm sat}^{-2.16}\,{\rm M}_\odot$, which is $4300\,{\rm M}_\odot$ for $\phi_{\rm sat} = 0.7$.

We have seen that most of the amplification of the field in the non-linear stage is due to compression, so that $B_{\rm rms}$ scales approximately as $\rho^{2/3}$ prior to equipartition ($\xi < \xi_{\rm eq}$); it follows that M_B is approximately constant during this phase. Under the assumption that the turbulent velocity remains about constant, after equipartition we have $B_{\rm rms}^2 = 4\pi\rho v_{\rm t}^2$ so that $M_B \propto \rho^{-1/2}$. To cover both cases, we note that equations (66) and (67) imply

$$B_{\rm rms}^2 = \min\left[\left(\frac{\xi}{\xi_{\rm eq}}\right)^{1/3}, 1\right] 4\pi\rho v_{\rm t}^2 \quad (73)$$

for pre- and post-equipartition, respectively. From equation (71), we then find that magnetic fields limit the mass that can undergo gravitational collapse to be at least

$$M_B = \left[\frac{3\chi(2\phi_{\rm t})^3}{16}\right]^{3/2}\left(\frac{\Omega_{\rm m}}{\Omega_{\rm b}}\right)^{1/2}\min\left[1, \left(\frac{\xi_{{\rm eq},i}}{\xi}\right)^{1/2}\right] M_{\rm m}, \quad (74)$$

$$M_B = 3470\,(2\phi_{\rm t})^3\min\left[(2\phi_{\rm t})^{3/2}, \left(\frac{4100}{\xi}\right)^{1/2}\right] M_{\rm m,6}\,{\rm M}_\odot, \quad (75)$$

where we set $\chi = 1/16$ and $\Omega_{\rm m} = 7.5\Omega_{\rm b}$ in the second equation. Note that equation (74) applies to present-day Giant Molecular Clouds (GMCs) for equipartition fields if $\xi_{\rm eq}$ is inserted from equation (67) and $\Omega_{\rm m}$ is set to $\Omega_{\rm b}$. Since $\phi_{\rm t} = v_{\rm t}/v_{\rm vir}$, the value of M_B is very sensitive to the turbulent velocity, $v_{\rm t}$. Prior to equipartition (first term in the above equations), M_B is constant, but for $\xi > \xi_{\rm eq}$ (second term), M_B varies as $\xi^{-1/2} \propto r^{k_\rho/2}$. In order for gravity to overcome magnetic fields for masses much less than $3500\,{\rm M}_\odot$, high densities are required; for example, reducing M_B below $100\,{\rm M}_\odot$ requires $n_{\rm H} \gtrsim 10^{6.5}\,{\rm cm}^{-3}$ for $\phi_{\rm t} \sim 1/2$ and $M_{\rm m,6} \sim z_{25} \sim 1$.

To compare with contemporary star formation, we recast these results in terms of the ratio of the gas mass inside r to the critical mass at that radius,

$$\mu_\Phi \equiv \frac{M(r)}{M_\Phi(r)} = \left[\frac{M(r)}{M_B}\right]^{1/3}. \quad (76)$$

Equation (74) then implies that

$$\mu_\Phi = \frac{4\xi^{(k_\rho-2)/2k_\rho}}{(2\phi_{\rm t})\sqrt{3}}\left(\frac{\Omega_{\rm b}}{\Omega_{\rm m}}\right)^{1/2}\max\left[\left(\frac{\xi_{\rm eq,i}}{\xi}\right)^{1/6}, 1\right]. \quad (77)$$

Just as in the case of equation (74) for M_B, this result applies to GMCs for equipartition fields if $\xi_{\rm eq}$ is inserted from equation (67) and $\Omega_{\rm m}$ is set to $\Omega_{\rm b}$. For the particular case $k_\rho = 2.2$ and $\phi_{\rm t} = 1/2$, equation (77) becomes

$$\mu_\Phi = 1.23\max\left[\left(\frac{4100}{\xi}\right)^{0.12}, \left(\frac{\xi}{4100}\right)^{0.045}\right]. \quad (78)$$

Note that the density dependence of μ_Φ is weak: The entire minihalo ($\xi = 1$) has $\mu_\Phi = 3.4$; the minimum value, $\mu_\Phi = 1.23$, occurs at the point that the gas first reaches equipartition ($\xi = 4100$); and ξ must exceed 2×10^{13} in order for μ_Φ to exceed 3.4. Over this entire density range, $\mu_\Phi \simeq 2 \pm 0.2$ dex.

As noted earlier, the field might saturate at a value that differs from the equipartition value by a factor of $\phi_{\rm sat}$, and correspondingly, μ_Φ would differ from the values given in equations (77) and (78) by a factor of $1/\phi_{\rm sat}$. The Mach number in the simulations of Abel et al. (2002) is of the order of 1/3, which is subsonic, so that $\phi_{\rm sat} \sim 0.7$ (Haugen et al. 2004; Federrath et al. 2011a) and $\mu_\Phi \sim 2/0.7 \sim 3$; the simulations of Greif et al. (2012) have Mach numbers ∼1, which would give a somewhat larger value of μ_Φ.

The results we have obtained for the magnetic fields in a minihalo are quite comparable to those for the fields in contemporary star-forming regions. Equation (68) shows that the field is in equipartition with turbulent motions at densities $\gtrsim 10^3$ cm^{-3}, comparable to the densities in molecular clumps today. As discussed earlier, equation (78) shows that the equipartition value of the mass-to-flux ratio is $\mu_\Phi \sim 2$, which is the value expected on theoretical grounds for Galactic GMCs (McKee 1989); at present, there is no direct measurement available for μ_Φ for GMCs. Star-forming clumps within GMCs have $\mu_\Phi \simeq$ 2–3 (Crutcher 2012; Li et al. 2015), which is also in good agreement with the predicted value in equation (78).

Krumholz & Federrath (2019) have recently reviewed the role of magnetic fields in contemporary star formation. For typical mass-to-flux ratios ($\mu_\Phi \sim$ 2–3), magnetic fields reduce the rate of star formation by a factor of a few. Magnetic fields have little direct effect on the peak of the IMF since radiative feedback is generally dominant. Magnetic fields reduce fragmentation, particularly in discs, which could suppress the formation of low-mass primordial stars that could survive until today. Reduced fragmentation also favours the production of massive stars. One of the main effects of magnetic fields is that if they are ordered, they produce outflows that reduce the typical stellar mass by a factor of ∼2–3. However, recent simulations show that no outflows are produced by turbulent magnetic fields (Gerrard, Federrath & Kuruwita 2019), so that effect should not be present in primordial star formation.

In sum, the kinematic dynamo is able to amplify the field from very small values (∼10^{-25} to 10^{-19} G) to moderate values (∼10^{-8} G), with very little of the amplification due to compression. On the other hand, the non-linear dynamo is much less efficient, providing an amplification of less than an order of magnitude in our example. The initial equipartition field of ∼10^{-4} G is attained with a compression somewhat less than 10^4, and we anticipate that the field will remain in approximate equipartition as the collapse continues to higher densities. During this phase of the collapse, the mass supported by the field against gravity, M_B, declines as $\xi^{-1/2}$ (equation 75) so that the mass-to-flux ratio in the core is nearly independent of density (equation 78). The equipartition field, as characterized by the ratio of the turbulent velocity to the virial velocity, $\phi_{\rm t} = v_{\rm t}/v_{\rm vir} \sim 1/2$, results in a normalized mass-to-flux ratio, μ_Φ, somewhat above unity. We estimate $\mu_\Phi \sim 3$ for subsonic turbulence, comparable to that in contemporary star-forming regions. As a result, magnetic fields could play a role in the formation of the first stars.

4 THEORY OF SIMULATIONS

One of the principal difficulties in simulating astrophysical fluids is that the physical viscosity is generally orders of magnitude smaller than the numerical viscosity, so that the actual Reynolds number is orders of magnitude larger than that in the simulation. For dynamos in minihaloes, the physical viscosity is set by collisions in neutral hydrogen and is $\nu \sim 10^{20}$ cm^2 s^{-1} for $T_3 \sim 1$ and $n_{\rm H} \sim 1$ cm^{-3} (Appendix A), whereas the numerical viscosity in SPH or grid-based codes is of the order of 10^{23} cm^2 s^{-1} for the same physical conditions and for resolutions corresponding to about 64 cells per Jeans length. As a result, the characteristic growth rate in the kinematic stage of the dynamo, $\sim\Gamma_\nu \propto \nu^{-1/2}$ (equation 6), is smaller by a factor of $\sim 10^{1.5}$. A corollary of this is that the time at which the dynamo enters the non-linear stage, $t_{\rm nl} \propto \Gamma_\nu^{-1}$ (equation 42), is larger by about the same factor. Thus, whereas the actual minihalo dynamo enters the non-linear stage prior to significant compression, simulated minihalo dynamos do so only after significant compression. We must therefore use the results for a dynamo in a time-dependent background given in Section 2.5.

Another important difference between the simulations considered here and reality is that we assume that the simulations are based on ideal MHD, so that the resistivity is numerical. As a result, the resistivity in the simulations is independent of B, whereas in the weakly ionized plasma that forms the first stars it is dominated by ambipolar diffusion and varies as B^2; the effect of this approximation is less significant than the large discrepancy between the simulated and actual viscosities, however.

The theoretically predicted evolution of the magnetic field shown in Fig. 1 is dramatically different from that in the simulations of Turk et al. (2012) and Stacy et al. (in preparation), principally due to the difference between the actual viscosity and that in the simulations. As noted by Sur et al. (2010) and Turk et al. (2012), the growth rate of the dynamo increases with the Reynolds number and therefore with resolution. [This follows directly from the growth rate of the kinematic dynamo $\Gamma \sim \Gamma_\nu$ (equation 6), and the fact that $\Gamma_\nu \propto Re^{1/2}$ (equations 3 and 4).] Here we seek to predict the outcome of a simulation of the evolution of the magnetic field in the formation of the first stars so that we can understand how it relates to the theoretical expectation described in the previous section and portrayed in Fig. 3.

4.1 SPH simulations of minihalo dynamos

We now estimate the outcome of an SPH simulation of a minihalo dynamo. The numerical viscosity for SPH is

$$\nu_{\rm sph} = 1.50 \times 10^{23} \left(\frac{h_{\rm f} m'^{1/3}_{\rm sph} T_3^{1/2}}{n_{\rm H}^{1/3}} \right) \ {\rm cm}^2 \ {\rm s}^{-1} \tag{79}$$

(equation C20), where $h_{\rm f}$ normalizes the SPH smoothing length (equation C16) and $m'_{\rm sph} = m_{\rm sph}/(1\,{\rm M}_\odot)$ is the normalized SPH particle mass. For example, Price (2012b) adopted $h_{\rm f} = 1.2$, whereas Stacy et al. (in preparation) adopted $h_{\rm f} = 3.63$; Price (2012b) did not need to adopt a value for $m_{\rm sph}$, but Stacy et al. (in preparation) adopted $m_{\rm sph} \simeq 0.03\,{\rm M}_\odot$ in the high-resolution portion of their run, corresponding to $h_{\rm f} m'^{1/3}_{\rm sph} = 1.13$; their simulation had about 3×10^7 particles representing the gas. As noted earlier, we expect the kinematic stage to extend well into the gravitational collapse of the star forming in the minihalo, and as a result, the effective outer scale of the turbulence is the Jeans length (Federrath et al. 2011b), $\lambda_{\rm J} = 386 (T_3/n_{\rm H})^{1/2}$ pc. The Reynolds number in the simulation of a gravitationally collapsing cloud is then

$$Re = \frac{\lambda_{\rm J} v_{\rm t}}{\nu_{\rm sph}} = 800 \left(\frac{v_{\rm t,5}}{h_{\rm f} m'^{1/3}_{\rm sph} n_{\rm H}^{1/6}} \right). \tag{80}$$

In order for a dynamo to operate, the magnetic Reynolds number, $R_{\rm m} = P_{\rm m} Re$, must exceed a critical value, $R_{\rm m,cr}$, as discussed in Section 2.2. We adopt the result of Haugen et al. (2004), $R_{\rm m,cr} \simeq 220 P_{\rm m}^{-1/2}$ for $0.1 \lesssim P_{\rm m} \lesssim 3$, so that

$$\frac{R_{\rm m}}{R_{\rm m,cr}} = 3.6 \left(\frac{P_{\rm m}^{3/2} v_{\rm t,5}}{h_{\rm f} m'^{1/3}_{\rm sph} n_{\rm H}^{1/6}} \right). \tag{81}$$

The maximum density for the operation of the dynamo is determined by setting this ratio equal to unity,

$$n_{\rm H,max} = 2.18 \times 10^3 \left(\frac{P_{\rm m}^{3/2} v_{\rm t,5}}{h_{\rm f} m_{\rm s}'^{1/3}} \right)^6 \ {\rm cm}^{-3}. \tag{82}$$

In Appendix C3, we estimate that the magnetic Prandtl number for grid-based codes is $P_{\rm m} \simeq 1.4$, and we adopt the same value for SPH codes. Then, for a typical turbulent velocity of 2 km s^{-1} (Greif et al. 2011), we find that the dynamo can operate only below a density of $n_{\rm H,max} \simeq 3 \times 10^6/(h_{\rm f} m_{\rm sph}'^{1/3})^6$ cm^{-3}. This is in the upper range of the densities in the SPH simulation of Stacy et al. (in preparation), which has $h_{\rm f} m_{\rm sph}'^{1/3} \simeq 1$.

In the kinematic phase of a simulated dynamo, the dynamo amplification factor is

$$\mathcal{A}_{\rm kin} = \exp\left(\frac{3}{8} \int_{t_0}^{t} \Gamma_\nu \, {\rm d}t' \right) \tag{83}$$

from equations (39) and (49). Here, we have taken $k_{\rm p}\ell_\nu \simeq 1$ in equation (39) since it lies between 1 and $P_{\rm m}^{1/2} \simeq 1$ (see the middle panel of Fig. 1). Since our focus is on dynamos in gravitationally collapsing clouds, we consider the case in which the growth rate varies as a power of the density, $\Gamma_\nu = \Gamma_{\nu 0} \xi^{q_\Gamma}$, where $\xi = \rho/\rho_0$ is the compression ratio and, in general, $x \propto \xi^{q_x}$. Recall that $\Gamma_\nu = (\epsilon/\nu)^{1/2}$ (equation 3) and $\epsilon = v_t^3/L$, so that if the outer scale of the turbulence is set by the Jeans length, then we have

$$q_\Gamma = \frac{1}{2}(q_\epsilon - q_\nu) = \frac{1}{2}\left(3q_\nu - \frac{1}{2} q_T + \frac{1}{2} - q_\nu \right). \tag{84}$$

Simulations (e.g. Greif et al. 2011) show that whereas there is some variation of $v_{\rm t}$ and T in the collapse, it is not systematic, so we shall generally treat them as constant and set $q_\nu = q_T = 0$. It follows that for SPH, $q_\nu = -1/3$ (equation 79), so that $q_\epsilon = 1/2$ and $q_\Gamma = 5/12$.

In Appendix B, we discuss the gravitational collapse of gas embedded in stationary dark matter. We consider the idealized case in which both the gas and the dark matter initially have spatially constant densities so that the density of the gas remains spatially constant when it undergoes free-fall collapse. We assume that the infall velocity is a factor of $\phi_{\rm ff}$ below the free-fall value so that the collapse time is $\phi_{\rm ff}$ times greater, where $t_{\rm ff,0} = (3\pi/32 G\rho_0)^{1/2}$ is the initial free-fall time in the absence of dark matter. The integral that appears in the dynamo amplification factor can be expressed as

$$\int_{t_0}^{t} \Gamma_\nu \, {\rm d}t' = \Gamma_{\nu 0} \phi_{\rm ff} t_{\rm ff,0} I_{q_\Gamma}(1, \xi) \tag{85}$$

in terms of the integral I_q evaluated in Appendix B; here, the density dependence of Γ_ν is given by $\Gamma_\nu \propto \xi^{q_\Gamma}$. Since the outer scale of the turbulence in a collapsing cloud is the Jeans length (Federrath et al. 2011b), it follows that the factor ϵ that enters Γ_ν is

$$\epsilon = \frac{v_{\rm t}^3}{\lambda_{\rm J}} = 8.40 \times 10^{-7} v_{\rm t,5}^3 \left(\frac{n_{\rm H}}{T_3} \right)^{1/2} \ {\rm cm}^2 \ {\rm s}^{-3}. \tag{86}$$

For the SPH viscosity given in equation (C20), we then have

$$\Gamma_{\nu 0} t_{\rm ff,0} = 3.33 \left(\frac{v_{\rm t,5}^{3/2}}{h_{\rm f}^{1/2} m_{\rm sph}'^{1/6} T_3^{1/2} n_{\rm H,0}^{(1/2)-q_\Gamma}} \right), \tag{87}$$

so that

$$\mathcal{A}_{\rm kin} = \exp\left[1.25 \left(\frac{\phi_{\rm ff} v_{\rm t,5}^{3/2}}{h_{\rm f}^{1/2} m_{\rm sph}'^{1/6} T_3^{1/2} n_{\rm H,0}^{(1/2)-q_\Gamma}} \right) I_{q_\Gamma}(1, \xi) \right] \tag{88}$$

from equations (83) and (85).

The growth of the field in a contracting medium is often characterized by the logarithmic derivative, ${\rm d}\ln B/{\rm d}\ln\rho$. For the kinematic stage of the dynamo, the field is $B = B_0(\rho/\rho_0)^{2/3}\mathcal{A}_{\rm kin}$ (equation 48). Since $\mathcal{A}_{\rm kin}$ is given by equation (83), we have

$$\frac{{\rm d}\ln B}{{\rm d}\ln\rho} = \frac{2}{3} + \frac{{\rm d}\ln \mathcal{A}_{\rm kin}}{{\rm d}t} \left(\frac{{\rm d}t}{{\rm d}\ln\rho} \right), \tag{89}$$

$$\frac{{\rm d}\ln B}{{\rm d}\ln\rho} = \frac{2}{3} + \frac{3}{8}\Gamma_\nu \left(\frac{r}{3|v|} \right), \tag{90}$$

where in the last step we used $\rho \propto r^{-3}$. Late in the collapse ($r \ll r_0$, $\xi^{1/3} \gg 1$), the velocity is $|v| \simeq v_{\rm g}(r_0/r)^{1/2} = v_{\rm g}\xi^{1/6}$ with $v_{\rm g} \sim r_0/t_{\rm ff,0}$ (see equations B8 and B9), so that

$$\frac{{\rm d}\ln B}{{\rm d}\ln\rho} = \frac{2}{3} + \frac{1}{4\pi}\phi_{\rm ff}\Gamma_{\nu 0} t_{\rm ff,0} \xi^{q_\Gamma - (1/2)}, \tag{91}$$

$$\frac{{\rm d}\ln B}{{\rm d}\ln\rho} = \frac{2}{3} + 0.26 \left(\frac{\phi_{\rm ff} v_{\rm t,5}^{3/2}}{h_{\rm f}^{1/2} m_{\rm sph}'^{1/6} T_3^{1/2} n_{\rm H,0}^{1/12}} \right) \xi^{q_\Gamma - (1/2)}. \tag{92}$$

So long as $q_\Gamma < 1/2$, the variation of B with ρ in the kinematic stage approaches $B \propto \rho^{2/3}$ at high densities – i.e. it is compression, not the dynamo, that amplifies the field then. As we shall see later, the slope is driven to 2/3 when the dynamo leaves the kinematic stage.

As an example, consider the case in which $v_{\rm t}$ and T do not have a systematic variation during the collapse (i.e. $q_\nu = q_T = 0$). As noted above equation (84), it follows that $q_\Gamma = 5/12$, so that equation (B17) gives

$$I_{5/12}(1, \xi) \simeq 2.43 \left(1 - 1.05\xi^{-1/12} \right) \quad \left(\xi^{1/3} \gg 1 \right), \tag{93}$$

where we have evaluated $I_{5/12}(1, \infty)$ numerically. For $v_{\rm t,5} \sim 2$, $n_{\rm H,0} \sim 1$ cm^{-3}, and $T_3 \sim 1$, we then find

$$\mathcal{A}_{\rm kin} \simeq \exp\left[\frac{8.6\phi_{\rm ff}}{h_{\rm f}^{1/2} m_{\rm sph}'^{1/6}} \left(1 - 1.05\xi^{-1/12} \right) \right] \quad \left(\xi^{1/3} \gg 1 \right). \tag{94}$$

The quantity $B/n_{\rm H}^{2/3}$, which is just $B_0\mathcal{A}_{\rm kin}$ in the kinematic stage, is plotted in Fig. 4(a) for three values of $\phi_{\rm ff}$, providing a graphic demonstration of the exponential sensitivity of the simulated dynamo to the input parameters. Note that for a kinematic dynamo, an increase in resolution at a fixed value of ξ (which is numerically the same as $n_{\rm H}$ in Fig. 4 since $n_{\rm H,0} = 1$ cm^{-3} there) is equivalent to an increase in $\phi_{\rm ff}$; for example, increasing the linear resolution by a factor of 2 corresponds to reducing $m_{\rm sph}$ by a factor of 8 and increasing $\phi_{\rm ff}$ by $\sqrt{2}$.

First, consider the case in which $\phi_{\rm ff} = 1$, so that the collapse occurs at the free-fall rate. This is sufficiently rapid that the dynamo cannot reach the non-linear stage before dynamo action is terminated because the density reaches $n_{\rm H,max}$ and $R_{\rm m}$ drops below the critical value. In this example, and for $h_{\rm f} m_{\rm s}'^{1/3} \simeq 1$, equation (94) gives an amplification factor for the kinematic dynamo of $\mathcal{A}_{\rm kin}(\xi_{\rm max}) \sim 10^{2.6}$, where $\xi_{\rm max} = n_{\rm H,max}/n_{\rm H,0} \simeq 3 \times 10^6$. The growth of the field by compression ($\xi_{\rm max}^{2/3} \simeq 10^{4.3}$) is much greater than the growth due to the dynamo ($\sim 10^{2.6}$). The slope of $B(\rho)$ is driven to 2/3 when the kinematic stage terminates. For $n_{\rm H} > n_{\rm H,max}$, the field grows by compression until it reaches equipartition. As shown in Fig. 4(a), which is based on the assumption that the initial field is $B_0 = 10^{-11}$ G, this occurs at a density of $\sim 10^{15}$ cm^{-3}, corresponding to $M/M_0 \sim 4 \times 10^{-6}$ for a power-law density profile with $k_\rho = 2.2$ (equation 72). For a minihalo with a gas mass of 4×10^4 M$_\odot$, the mass that reaches equipartition is very small, ~ 0.2 M$_\odot$. Thus, in this case, the magnetic field has a negligible effect throughout most of the core, at least up

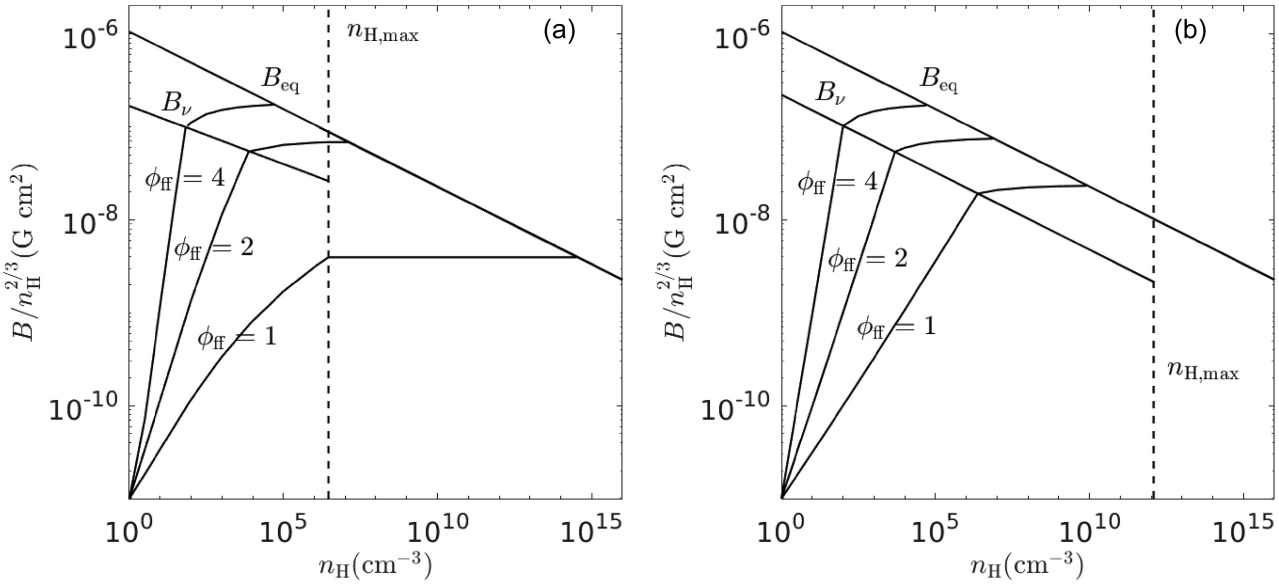

Figure 4. The expected value of $B/n_{\rm H}^{2/3}$ for SPH (a) and grid-based (b) simulations of the gravitational collapse of a turbulent gas in a dark matter minihalo. Illustrated are cases in which the collapse occurs at the free-fall rate ($\phi_{\rm ff}=1$), half that rate ($\phi_{\rm ff}=2$), and a quarter of that rate ($\phi_{\rm ff}=4$). The equipartition field, $B_{\rm eq}=(4\pi\rho v_{\rm t}^2)^{1/2}$, and the field at which non-linear effects become important at the viscous scale, $B_\nu=(4\pi\rho v_\nu^2)^{1/2}$, both normalized by $n_{\rm H}^{2/3}$, are also plotted. The initial field and density are $B_0=10^{-11}$ G and $n_{\rm H,0}=1$ cm^{-3}, and we adopt $T=10^3$ K and $v_{\rm t}=2$ km s^{-1}. The magnetic Prandtl number for simulations is taken to be $P_{\rm m}=1.4$ (Appendix C). In reality (Fig. 3), the magnetic field begins at a value well below the minimum in this figure, intersects the non-linear curve (B_ν) at $n_{\rm H}\simeq 1$ cm^{-3}, and then bends over to become nearly horizontal before intersecting the equipartition line ($B_{\rm eq}$). (a) The SPH simulation is assumed to have $h_{\rm f}m_{\rm s}'^{1/3}=1$ (see Appendix C2). For $\phi_{\rm ff}=1$, the kinematic dynamo amplifies the field until the magnetic Reynolds number drops to the critical value below which the dynamo ceases, which occurs at a density $n_{\rm H,max}$. For $\phi_{\rm ff}=2$ or 4, the field becomes non-linear on the viscous scale ($B=B_\nu$). In any case, the non-linear dynamo does not have much time to operate, so the field then grows primarily by compression in the non-linear stage until it reaches equipartition with the turbulence. Subsequently, the field remains in approximate equipartition. (b) As in the SPH case, the non-linear dynamo does not have much time to operate, so the growth of the field in this stage is primarily by compression. The maximum density at which the dynamo can operate based on the condition $R_{\rm m}<R_{\rm m,cr}$ is $n_{\rm H,max}=1.2\times10^{12}$ cm^{-3} for the resolution of the AMR (adaptive mesh refinement) simulation of Stacy et al. (in preparation).

to the time that the protostar begins to form. If the initial field were less than 10^{-11} G, the magnetic field would be even less important.

Next consider the case $\phi_{\rm ff}=2$, in which the collapse occurs at half the free-fall rate so that the dynamo has more time to act. In this case, the field grows to B_ν before the density reaches $n_{\rm H,max}$. At this point, the Alfvén velocity $v_{\rm A}$ equals the velocity of the viscous scale eddies, $v_\nu=(\epsilon\nu)^{1/4}$ (equation 3), so that

$$B_\nu=(4\pi\rho)^{1/2}v_\nu=1.00\times10^{-7}\left(h_{\rm f}m_{\rm s}'^{1/3}\right)^{1/4}v_{\rm t,5}^{3/4}n_{\rm H}^{13/24}\,{\rm G}, \tag{95}$$

which is plotted in Fig. 4(a). Since $v_{\rm A}=v_{\rm A0}\mathcal{A}_{\rm kin}\xi^{1/6}$ up to the point that B reaches B_ν (equation 48), the compression required for the field to reach B_ν is

$$\xi_\nu=\left(\frac{v_\nu}{v_{\rm A0}\mathcal{A}_{\rm kin}}\right)^6=\left(\frac{v_{\nu0}}{v_{\rm A0}\mathcal{A}_{\rm kin}}\right)^{12/[2-3(q_\epsilon+q_\nu)]}, \tag{96}$$

where we used $v_\nu=v_{\nu0}\xi^{(q_\epsilon+q_\nu)/4}$ in the second expression. The exponential dependence on the uncertain parameters in $\mathcal{A}_{\rm kin}$ that describe the collapse (see equation 94) means that ξ_ν is essentially unpredictable for simulations with a numerical viscosity several orders of magnitude larger than the actual one, as is generally the case. By contrast, ξ_ν is well determined in Nature: the small viscosity means that the exponent in the expression for $\mathcal{A}_{\rm kin}$ (equation 88) is large enough to make $\xi_\nu\simeq1$ (Section 3). For the hypothetical simulation with $\phi_{\rm ff}=2$ shown in Fig. 4(a), the field reaches B_ν at $\xi_\nu\simeq10^4$ with $\mathcal{A}_{\rm kin}\simeq10^{3.7}$, so that the dynamo amplification is an order of magnitude greater than that due to compression. On the other hand, for $\phi_{\rm ff}=4$ the field reaches B_ν at $\xi_\nu\simeq80$, and the dynamo amplification $\mathcal{A}_{\rm kin}\simeq10^4$ is almost three orders of magnitude greater than the factor $\simeq$20 due to compression.

After reaching B_ν, the dynamo enters the non-linear stage. The non-linear amplification factor is given by (equations 51 and B17)

$$\mathcal{A}_{\rm nl}^2=1+2\chi\phi_{\rm ff}\Gamma_{\nu0}t_{\rm ff,0}\xi_\nu^{(1/3)-(1/2)(q_\epsilon+q_\nu)}I_{q_\epsilon-(1/3)}(\xi_\nu,\xi), \tag{97}$$

$$\mathcal{A}_{\rm nl}^2\simeq1+\frac{0.088}{(5/6)-q_\epsilon}\left(\frac{\phi_{\rm ff}v_{\rm t,5}^{3/2}}{h_{\rm f}^{1/2}m_{\rm sph}'^{1/6}T_3^{1/2}n_0^{1/12}}\right)\xi_\nu^{q_\Gamma-(1/2)}\times\left[1-\left(\frac{\xi_\nu}{\xi}\right)^{(5/6)-q_\epsilon}\right]\quad\left(\xi_\nu^{1/3}\gg1\right), \tag{98}$$

where we used equation (84) for q_Γ and equation (96) for ξ_ν. This equation applies only for $\xi<\xi_{\rm max}$ since the dynamo cannot operate at higher densities. In the absence of systematic variations in T or $v_{\rm t}$, we have $q_\epsilon=1/2$ and $q_\Gamma=5/12$, so $\mathcal{A}_{\rm nl}$ is typically $\sim$1. For example, the case portrayed in Fig. 4 has $\mathcal{A}_{\rm nl}^2\simeq1+0.75\phi_{\rm ff}\xi_\nu^{-1/12}$ for $(\xi_\nu/\xi)^{1/3}\ll1$. As a result, the non-linear amplification of the field is primarily due to compression of the field. The fact that $\mathcal{A}_{\rm nl}$ is smaller for simulations than for the physical case is expected since $\mathcal{A}_{\rm nl}\propto Re^{1/4}$ (see below equation 52) and Re is much smaller for simulations.

The dynamo reaches equipartition at $\xi_{\rm eq}$. However, just as in the case of ξ_ν, the uncertainty in $\mathcal{A}_{\rm kin}$ means that we cannot predict the equipartition density or field in a simulation with any certainty. In

equipartition, we have $v_A = v_t$, so that

$$\xi_{eq} = \left(\frac{v_t}{v_{A0}\mathcal{A}_{eq}}\right)^6, \tag{99}$$

where $\mathcal{A}_{eq} = \mathcal{A}_{kin}\mathcal{A}_{nl}(t_{eq})$ is the amplification factor at the time that the field reaches equipartition. In Fig. 4(a), we know all the parameters. For $\phi_{ff} = 2$, for example, the field reaches equipartition at $n_H \simeq 1.2 \times 10^7$ cm^{-3}, when $B \simeq 4 \times 10^{-3}$ G. Keep in mind that these values are based on the assumption that $B_0 = 10^{-11}$ G; if the initial field were weaker, it would reach equipartition at a higher density with a correspondingly higher value of the field strength. The field then remains in equipartition and grows as $n_H^{1/2}$. As discussed in Section 3.5, equipartition fields with $\phi_t \sim 1/2$ result in mass-to-flux ratios $\mu_\Phi \sim 2$–3, which are small enough that magnetic fields can significantly affect star formation. Note that the full effect of this low mass-to-flux ratio is felt only in the central 3×10^{-3} of the core for $\xi_{eq} \sim 10^7$ (equation 72), or about 100 $M_\odot$ for a minihalo with a gas mass of 4×10^4 $M_\odot$. If the field saturates at a value ϕ_{sat} less than the equipartition value (equation 70), then it would saturate at a density ϕ_{sat}^6 less than that in equation (99), corresponding to a mass $\phi_{sat}^{-2.16}$ times greater; for $\phi_{sat} = 0.7$ (Federrath et al. 2011a), this is about a factor of 2.

We conclude that SPH simulations can follow a significant growth of the field in a gravitational collapse due to the action of a small-scale dynamo, but the mass in which the field reaches equipartition is small compared to the correct value and it is difficult to predict the final field in advance. The results presented here will be compared with SPH simulations in Paper II.

4.2 Grid-based simulations of minihalo dynamos

Grid-based simulations of minihalo dynamos are quite similar to SPH simulations, except that the numerical viscosity is somewhat different (Appendix C). Since the kinematic stage extends well into the gravitational collapse due to the large value of the viscosity, the outer scale of the turbulence is the Jeans length, as for the SPH case. The Reynolds number is then given by $Re = 512/(64J_{max})^{4/3}$ (equation C13), where J_{max} is the maximum value of the ratio of the grid size to the Jeans length allowed in the adaptive mesh simulation. The ratio of the magnetic Reynolds number to the critical value, $R_{m,cr} = 220/P_m^{1/2}$ (see the comment above equation 81), is then

$$\frac{R_m}{R_{m,cr}} = 2.33 P_m^{3/2}\left(\frac{1/64}{J_{max}}\right)^{4/3} \tag{100}$$

with the aid of equation (C13). As discussed in Appendix C, this implies that that the dynamo can operate ($R_m > R_{m,cr}$) for $\lambda_J/\Delta x >$ 16–32, as found by Federrath et al. (2011b), provided P_m is in the range 1–2. More precisely, the dynamo can operate provided

$$J_{max} < 0.03 P_m^{9/8}, \tag{101}$$

which is 1/23 for our adopted value $P_m = 1.4$. For a given grid size, Δx, the maximum density is the Truelove–Jeans density, $\rho_{TJ} = \pi J_{max}^2 c_s^2/(G\Delta x^2)$ (equation C10). Equation (101) then sets the maximum density for a dynamo to operate in a grid-based simulation,

$$n_{H,max} = 1.23 \times 10^{11}\left(\frac{P_m^{9/4}T_3}{\Delta x_{14}^2}\right) \text{ cm}^{-3}, \tag{102}$$

where $\Delta x_{14} = \Delta x/(10^{14}$ cm). The highest resolution in the grid-based simulation of Stacy et al. (in preparation) is $\Delta x = 0.47 \times 10^{14}$ cm. This gives $n_{H,max} = 1.2 \times 10^{12}$ cm^{-3}, slightly less than the maximum density in their simulation. The fact that $n_{H,max}$ is much larger in the grid-based simulation than in the SPH simulation of Stacy et al. (in preparation) was by design: the grid-based simulation was a zoom-in on the cosmological SPH simulation.

The dynamo amplification factor in the kinematic stage is given by equation (83). Using the grid-based viscosity from equation (C14), which has $\nu_g \propto v_t(T/n_H)^{1/2}$, we have $\Gamma_\nu \propto \mathcal{M}n_H^{1/2}$ so that

$$\Gamma_\nu t_{ff,0} = 6.93\left(\frac{1/64}{J_{max}}\right)^{2/3}\mathcal{M}\xi^{1/2}, \tag{103}$$

where $\mathcal{M} = v_t/c_s$ is the turbulent Mach number. In terms of $\langle\mathcal{M}\rangle$, the weighted average value of the Mach number over the range of compression ratios from 1 to ξ, equations (83) and (47) then imply

$$\mathcal{A}_{kin} = \exp\left[2.60\phi_{ff}\left(\frac{1/64}{J_{max}}\right)^{2/3}\langle\mathcal{M}\rangle I_{1/2}(1,\xi)\right], \tag{104}$$

where $I_{1/2} \simeq (2/3\pi)\ln\xi$ (equation B19). As in the case of SPH, the value of $\mathcal{A}_{kin}$ is very sensitive to the input parameters: Fig. 4(b) shows the significant differences resulting from a factor of 2 difference in ϕ_{ff}. Just as in the case with SPH simulations, grid-based simulations of gravitational collapse can follow large amplifications of the field provided the resolution is high ($J_{max} \lesssim 1/64$), but the amplification cannot be predicted in advance with any accuracy. For the kinematic stage of the dynamo, an increase in resolution at a fixed value of ξ is equivalent to an increase in ϕ_{ff} in determining the magnitude of the kinematic amplification: doubling the linear resolution (reducing J_{max} by a factor of 2) is equivalent to increasing ϕ_{ff} by a factor of $2^{2/3}$. The effects of an increase in resolution on a kinematic dynamo can thus be inferred from Fig. 4.

The logarithmic slope of $B(\rho)$ is given by equation (91). For grid-based simulations, we have $q_\Gamma = (1/2) + q_\mathcal{M}$ from equation (103), so that

$$\frac{d\ln B}{d\ln\rho} = \frac{2}{3} + 0.55\phi_{ff}\mathcal{M}_0\left(\frac{1/64}{J_{max}}\right)^{2/3}\xi^{q_\mathcal{M}}. \tag{105}$$

Note that the slope grows without bound as the resolution increases – i.e. as J_{max} and $\nu_g \propto J_{max}^{4/3}$ decrease. Indeed, as discussed in Section 3, a viscosity as small as the actual viscosity allows the kinematic dynamo to amplify the field by many orders of magnitude before the density changes significantly.

The dynamo leaves the kinematic stage of evolution when the field reaches the value

$$B_\nu = (4\pi\rho)^{1/2}v_\nu = 1.11 \times 10^{-7}\left(\frac{J_{max}}{1/64}\right)^{1/3} v_{t,5}n_H^{1/2}\text{ G}, \tag{106}$$

which is plotted in Fig. 4(b). The discussion of the values of ξ_ν and ξ_{eq}, which mark the onset of the non-linear stage and reaching equipartition, respectively, is similar to that in the previous section for the $\phi_{ff} = 2$ and 4 cases in SPH (for which $n_{H,max}$ plays no role): The exponential uncertainty in $\mathcal{A}_{kin}$ implies that these quantities are essentially indeterminate in advance. Of course, if one specifies the uncertain parameters, one can describe the kinematic dynamo accurately. For $\langle\mathcal{M}\rangle = 1$ and $v_{t,5} = 2$, one can show with the aid of equation (104) that $\mathcal{A}_{kin}(\xi_\nu)$ ranges from $10^{3.3}$ for $\phi_{ff} = 1$ to 10^4 for $\phi_{ff} = 4$. The values of ξ_ν are 2.4×10^6 and 100, respectively, so compression dominates dynamo amplification by an order of magnitude in the first case, but is relatively minor in the second.

We now consider the non-linear evolution of the dynamo in a grid-based simulation. From the discussion above equation (103), we have $q_\Gamma = q_\mathcal{M} + (1/2)$; simulations (e.g. Greif et al. 2012; Stacy et al., in preparation) show that the Mach number is approximately constant over a large range of densities in the collapse so that $q_\mathcal{M} \sim 0$. The

non-linear amplification factor (equation 97) then becomes

$$\mathcal{A}_{\rm nl}^2 \simeq 1 + \frac{0.18\phi_{\rm ff}\mathcal{M}_0}{(5/6) - q_\epsilon}\left(\frac{1/64}{J_{\rm max}}\right)^{2/3} \xi_v^{q_\mathcal{M}} \times \left[1 - \left(\frac{\xi_v}{\xi}\right)^{(5/6)-q_\epsilon}\right] \quad \left(\xi_v^{1/3} \gg 1\right). \tag{107}$$

The exponent $q_\epsilon \simeq 1/2$ if there is no systematic variation of velocity or temperature in the collapse ($q_v \simeq q_T \simeq 0$; see equation 84). For grid-based codes, non-linear dynamo amplification is small (as it is for SPH codes) provided the Mach number does not increase with compression ($q_\mathcal{M} \lesssim 0$). For the case shown in Fig. 4(b) ($\mathcal{M}_0 = 1$, $q_\epsilon = 1/2$, $q_\mathcal{M} = 0$, and $J_{\rm max} = 1/64$), the amplification factor for the energy is $\mathcal{A}_{\rm nl}^2 = 1 + 0.55\phi_{\rm ff}$. Equation (99) then implies that the field reaches equipartition at $\xi_{\rm eq} \simeq (8 \times 10^9,\ 7 \times 10^6,\ 5 \times 10^4)$ for $\phi_{\rm ff} = (1, 2, 4)$, respectively. If the field saturates at a value $\phi_{\rm sat} = 0.7$ times smaller than the equipartition field (Federrath et al. 2011a), then these values are reduced by a factor of 8.5. For a density power law $k_\rho = 2.2$, the field is saturated in the central (11, 140, 800) $M_\odot$, respectively.

4.2.1 Comparison with Federrath et al. (2011b)

As noted earlier, uncertainties in the parameters prevent an accurate prediction of the amplification of the field in the kinematic stage of the dynamo. However, once the simulation has been done, it is possible to compare our theoretical estimates with the results of the simulation. Here, we compare with the simulation of a kinematic dynamo in a gravitationally collapsing cloud by Federrath et al. (2011b). Their simulations covered the range $J_{\rm max} = 1/8$ to 1/128, and they found dynamo action for $J_{\rm max} = 1/32$ but not for 1/16. They presented their results in terms of the time normalized by the free-fall time, $d\tau_{\rm F} = dt/t_{\rm ff}$, so that (equation B13)

$$\tau_{\rm F} = \frac{1}{t_{\rm ff,0}}\int_{t_0}^{t} \xi^{1/2}\, dt = \phi_{\rm ff} I_{1/2}(1, \xi). \tag{108}$$

(Note that their simulations did not include dark matter, so $I_{1/2} \simeq (2/3\pi)\ln(64\xi)$ for $\xi^{1/3} \gg 1$.) Federrath et al. (2011b) show that their results at late times imply $B/\rho^{2/3} \propto \mathcal{A}_{\rm kin}$ varies as $\exp(\Omega\tau_{\rm F})$. We find

$$\Omega = 2.60\left(\frac{1/64}{J_{\rm max}}\right)^{2/3}\langle\mathcal{M}\rangle \tag{109}$$

from equation (104). Over the normalized time interval from $\tau_{\rm F} = 8$ to $\tau_{\rm F} = 12$, the Mach number in the inner part of their simulation increases by a factor of 2 and has a typical value $\mathcal{M} \simeq 0.5$. We therefore predict $\Omega \simeq 1.3[(1/64)/J_{\rm max}]^{2/3}$.

How does this compare with their results? First of all, they find that $\mathcal{A}_{\rm kin} \propto \exp(\Omega\tau_{\rm F})$ at late times, with $\Omega =$ const in a given simulation; we predict that $\Omega \propto \langle\mathcal{M}\rangle$, which is nearly constant (their numerical results imply $\langle\mathcal{M}\rangle \simeq (\mathcal{M}_0\mathcal{M})^{0.5} \propto \xi^{0.05}$ approximately). The values they found, $\Omega = 0.4$ at $J_{\rm max} = 1/64$ and 0.5 at $J_{\rm max} = 1/128$, are somewhat less than the values we predict. In agreement with their theoretical analysis, we predict that $\Omega \propto Re^{1/2}$ (equations 109 and C13), but as they point out, this does not agree with their numerical results, which are close to $\Omega \propto Re^{0.3}$ for constant $P_{\rm m}$. We note that our result follows from having the growth rate vary as $\nu^{-1/2}$ (Section 2) and having the numerical viscosity for grid-based codes vary as $\Delta x^{4/3}$ (Appendix C), both of which appear reasonable. It is possible that the actual scaling of Ω with $J_{\rm max}$ (or, equivalently, Re) appears only at higher resolution.

5 CONCLUSIONS

Magnetic fields affect the fragmentation of gravitationally collapsing gas, and that in turn affects the IMF. This is particularly important for the first stars since it determines the nucleosynthesis that results when the stars explode as SNe and whether Pop III stars can form with low enough masses that they survive today. As discussed in the Introduction, a great deal of work has been done on the origin of primordial magnetic fields. In the absence of any observational data, their role in the formation of the first stars must come through theory and simulation. The aim of this paper has been to make a theoretical estimate of the magnitude of the field in regions where the first stars formed and then compare that with the results that are expected from simulations, given that the numerical viscosity and resistivity are orders of magnitude larger than the actual values. In a companion paper (Stacy et al., in preparation), we describe the results of a simulation of the formation of the first stars that includes magnetic fields.

As discussed in the Introduction, it has been realized for some time that small-scale dynamos can produce dynamically important magnetic fields in regions of Pop III star formation. Dynamos require seed fields, and a great deal of effort has gone into determining possible mechanisms for generating such fields. Mechanisms that might have occurred in the early Universe, such as those due to inflation or phase transitions, are very uncertain. The one mechanism that depends only on known physics is the Biermann battery (Biermann 1950; Biermann & Schlüter 1951), which can produce fields of $\sim 10^{-24.5}$ G throughout the IGM after recombination (Naoz & Narayan 2013) and $\sim 10^{-19}$ G in newly formed galaxies (Biermann & Schlüter 1951). Such fields must be amplified by small-scale dynamos in a turbulent medium to become dynamically or observationally significant. Observations of gamma-rays from blazars set a lower limit of 10^{-17} G on intergalactic magnetic fields with a correlation length exceeding 1 Mpc, with larger values for smaller correlation lengths (Neronov & Vovk 2010; Taylor et al. 2011), although this result has recently been called into question (Broderick et al. 2018; Alves Batista et al. 2019).

The overall conclusion of our analysis is that a small-scale dynamo can amplify primordial fields created by the Biermann battery mechanism to the point that the dynamo enters the non-linear stage and that subsequent compression brings the field into approximate equipartition with the turbulent motions in the collapsing gas cloud. However, because the numerical viscosity is typically orders of magnitude greater that the actual value, the field in a simulation becomes dynamically significant in a much smaller mass than in reality. We now separately summarize our results for the fields expected theoretically and those expected in numerical simulations.

(1) *The Biermann battery* generates weak magnetic fields ($\sim 10^{-4}\omega$, where $\omega = \nabla \times \boldsymbol{v}$ is the vorticity) due to forces that produce unequal accelerations of the electrons and ions and have a curl, such as non-parallel pressure and density gradients. We confirmed the statement by Kulsrud et al. (1997) that dissipative processes in shocks do not significantly affect the operation of the Biermann battery. Standard estimates for the Biermann field are based on the vorticity produced by curved shocks on galactic scales and give values of $\sim 10^{-19}$ G (Biermann & Schlüter 1951; Pudritz & Silk 1989), and we find a similar value for cosmic minihaloes. We show that the subsequent turbulent cascade gives fields on the viscous scale in cosmic minihaloes ($\sim$0.01 pc) of the order of 10^{-16} G.

(2) *The small-scale dynamo.* We summarized some of the key results on small-scale dynamos, which begin by amplifying fields on the viscous scale (or resistive scale, if that is larger). Extensive

theoretical work and simulations have shown that turbulence can amplify weak magnetic fields until they reach approximate equipartition (provided the magnetic Reynolds number, $R_{\rm m} = Lv_L/\eta$, is large enough – see equation 25). For magnetic Prandtl numbers exceeding unity ($P_{\rm m} = \nu/\eta > 1$, where ν is the viscosity and η is the resistivity), the largest fields are on subviscous scales until equipartition is reached on the viscous scale; we label that field B_ν. Subsequently, both the magnitude and the scale of the field grow as it reaches equipartition with larger and larger eddies. In the post-recombination Universe, ambipolar diffusion provides the dominant resistivity for fields $B \gtrsim 10^{-13} n_{\rm H}$ G (Appendix A). We followed the treatment of Xu & Lazarian (2016) in treating non-ideal effects on the dynamo, summarizing their results on the complex behaviour of the dynamo in two figures, one for the case of Ohmic resistivity (Fig. 1) and one for resistivity due to ambipolar diffusion (Fig. 2). The field grows exponentially in the kinematic phase of the dynamo ($B < B_\nu$) and as $t^{1/2}$ in the non-linear phase ($B > B_\nu$) provided $P_{\rm m}(B_\nu)$ is not too small. The values of the parameters describing dynamos in minihaloes are summarized in Table 1.

(3) *Dynamos in a time-dependent medium.* The magnetic Reynolds number in a typical cosmic minihalo is large (see Table 1), so flux freezing is a good approximation for the effects of compression. We determine the growth of the field in a time-dependent medium due to both compression, $B \propto \rho^{2/3}$, and the dynamo. Because the growth rate of the field in the non-linear stage of the dynamo is much less than that of the kinematic dynamo, compression generally dominates dynamo amplification of the field in the non-linear stage. On the other hand, dynamo amplification is relatively more important for the specific magnetic energy, $\mathcal{E}_B = B^2/8\pi\rho$, and as a result, the non-linear dynamo generally amplifies the magnetic field energy to the point that it is within an order of magnitude of equipartition in a gravitational collapse, even in the absence of compression.

(4) *Gravitational collapse.* In a cold dark matter universe, the first stars form via the gravitational collapse of gas in a cosmic minihalo. In Appendix B, we first develop an approximation for the free-fall collapse of a constant-density sphere; our analytical expression for $r(t)$ is complementary to the approximation for $t(r)$ obtained by Girichidis et al. (2014). We then idealize the contraction of the baryons in the minihalo as a free-fall collapse of uniform density sphere of gas in a static dark matter halo of constant density and show that the dark matter accelerates the collapse by slightly more than a factor of 2.

(5) *Theoretically predicted magnetic field in the formation of the first stars.* The evolution of a dynamo in a collapsing minihalo depends on a large number of parameters: the initial density, $n_{\rm H,0}$, the turbulent velocity, $v_{\rm t}$ (which we parametrize in terms of the virial velocity, $v_{\rm t} = \phi_{\rm t} v_{\rm vir}$), the temperature, T, the mass of the collapsing cloud, M_0, the rate of collapse (parametrized by $\phi_{\rm ff}$), and the rate at which these quantities vary with density (denoted by q_x for quantity x). (The initial value of the field, B_0, enters only logarithmically, and is important only if it is many orders of magnitude less than our estimate of $\sim 10^{-16}$ G.) Choosing values of these parameters that are consistent with simulations (e.g. those of Greif et al. 2012), we find that the time for the field to grow from its initial amplitude of $\sim 10^{-16}$ G to equipartition at the viscous scale, $B_\nu \sim 10^{-8}$ G, is less than the virial time in the minihalo; hence, the exponential growth of the field occurs at approximately constant gas density. This rapid growth of the field is consistent with that found in previous work (e.g. Schleicher et al. 2010; Schober et al. 2012b). The subsequent non-linear dynamo amplification is sufficient to bring the field energy to within about an order of magnitude of equipartition; none the less, the overall amplification of the field is generally dominated by compression. We estimate that the field first reaches equipartition with turbulent velocities of the order of 2 km s^{-1} (taken from simulations) at a value of $\sim 10^{-4}$ G; the field subsequently grows as $n_{\rm H}^{1/2}$. The field reaches equipartition with the central 5 per cent of the mass of the gas. Our conclusion that the field reaches equipartition in a minihalo at $z \sim 25$ differs from that of Xu & Lazarian (2016), who found that equipartition was not reached until a time of about 6×10^8 yr (the age of the Universe at $z \simeq 8$) since they did not consider the increase in density that occurs in star formation.

(6) *Magnetic effects on the first stars.* The ratio of the mass-to-flux ratio to the critical value, μ_Φ, is predicted to be about 2–3. Magnetic fields in contemporary star formation regions are also in approximate equipartition and have similar values of μ_Φ (Crutcher 2012), so magnetic fields could play an important role in the formation of the first stars. The fields in regions of first-star formation were produced in a turbulent small-scale dynamo and lack large-scale order, in contrast to those in regions of contemporary star formation, and as a result, protostellar outflows are unlikely from the first stars.

We then discussed the possible outcome of simulations of the growth of magnetic fields in the formation of a primordial star in a minihalo, using either an SPH or a grid-based ideal MHD code. The viscosity and resistivity in the simulations are assumed to be purely numerical.

(1) *Numerical viscosity and resistivity.* We developed a method of estimating the numerical viscosity, ν, that is in agreement with the estimate of Benzi et al. (2008) for grid-based codes and of Bauer & Springel (2012) for SPH codes. The value of the numerical viscosity in current simulations is typically more than 1000 times greater than the actual viscosity in weakly ionized primordial gas. We estimate that the magnetic Prandtl number is $P_{\rm m} = \nu/\eta \sim 1.4$ for grid-based codes based on the results of Federrath et al. (2011b); we adopt the same value for SPH codes.

(2) *Suppression of the dynamo by numerical resistivity.* Dynamos cannot operate if the magnetic Reynolds number, $R_{\rm m}$, is too small. We determined the maximum density, $n_{\rm H,\,max}$, at which dynamos can operate for both SPH and grid-based AMR codes under the assumption that the length scale in the Reynolds number is set by the Jeans length (equations 82 and 102). Low values of $n_{\rm H,\,max}$ lead to high values of the density at which the field reaches equipartition and therefore small fractions of the collapsing mass in which the field is dynamically significant.

(3) *Predicted magnetic fields in simulations of gravitational collapsing gas.* The large value of the numerical viscosity for a resolution of 64 cells per Jeans length ($J = 1/64$), a typical value in current simulations, implies that the growth rate of the kinematic dynamo is $\lesssim 1/30$ of the physically correct value. As a result, the growth of the field by compression is predicted to exceed that due to the dynamo if the collapse occurs at the free-fall rate ($\phi_{\rm ff} \simeq 1$). After the dynamo enters the non-linear stage, dynamo amplification is predicted to be relatively less important compared to compression in simulations than in reality. As noted earlier, the evolution of the dynamo depends on a number of parameters; in simulations, the resolution is an additional important parameter. The total amplification in the kinematic stage of the dynamo is exponentially dependent on these parameters, so the growth of the field in a simulation is difficult to predict in advance. Examples of the predicted outcomes of simulations of the growth of magnetic fields in a gravitationally collapsing cloud are given in Fig. 4. Increasing the resolution of the simulation increases the mass fraction in which the field can reach equipartition.

ACKNOWLEDGEMENTS

We thank Siyao Xu for extensive discussions on her work and for comments on drafts of this paper. We thank Robi Banerjee, Eric Blackman, Christoph Federrath, Robert Fisher, Alex Lazarian, Alex Schekochihin, Zack Slepian, Volker Springel, and Terrence Tricco for helpful comments, and Andrew Cunningham for sharing data analysis routines with us. We also thank the referee, Jennifer Schober, whose recommendations significantly improved the paper. This research was supported in part by the National Science Foundation though grant AST-1211729 and by the National Aeronautics and Space Administration through ATP grants NNX13AB84G and NNX17AK39G.

DATA AVAILABILITY

No new data were generated or analysed in support of this research.

REFERENCES

Abel T., Bryan G. L., Norman M. L., 2002, Science, 295, 93
Alvarez M. A., Bromm V., Shapiro P. R., 2006, ApJ, 639, 621
Alves Batista R., Saveliev A., de Gouveia Dalpino E. M., 2019, MNRAS, 489, 3836
Balbus S. A., 1993, ApJ, 413, L137
Banerjee R., Jedamzik K., 2004, Phys Rev. D, 70, 123003
Barkana R., Loeb A., 2001, Phys. Rep., 349, 125
Batchelor G. K., 1950, Proc. R. Soc. Lond. A, 201, 405
Bauer A., Springel V., 2012, MNRAS, 423, 2558
Beck R., Brandenburg A., Moss D., Shukurov A., Sokoloff D., 1996, ARA&A, 34, 155
Benzi R., Biferale L., Fisher R. T., Kadanoff L. P., Lamb D. Q., Toschi F., 2008, Phys. Rev. Lett., 100, 234503
Beresnyak A., 2012, Phys. Rev. Lett., 108, 035002
Biermann L., 1950, Z. Naturforsch. A, 5, 65
Biermann L., Schlüter A., 1951, Phys. Rev., 82, 863
Brandenburg A., 2014, ApJ, 791, 12
Brandenburg A., Zweibel E. G., 1994, ApJ, 427, L91
Broderick A. E., Tiede P., Chang P., Lamberts A., Pfrommer C., Puchwein E., Shalaby M., Werhahn M., 2018, ApJ, 868, 87
Bromm V., 2013, Rep. Prog. Phys., 76, 112901
Bromm V., Loeb A., 2004, New Astron., 9, 353
Bromm V., Coppi P. S., Larson R. B., 2002, ApJ, 564, 23
Chen K.-J., Whalen D. J., Wollenberg K. M. J., Glover S. C. O., Klessen R. S., 2017, ApJ, 844, 111
Cho J., Vishniac E. T., Beresnyak A., Lazarian A., Ryu D., 2009, ApJ, 693, 1449
Clark P. C., Glover S. C. O., Klessen R. S., 2008, ApJ, 672, 757
Clark P. C., Glover S. C. O., Klessen R. S., Bromm V., 2011, ApJ, 727, 110
Crutcher R. M., 2012, ARA&A, 50, 29
Davies G., Widrow L. M., 2000, ApJ, 540, 755
Draine B. T., 1980, ApJ, 241, 1021
Draine B. T., Roberge W. G., Dalgarno A., 1983, ApJ, 264, 485
Durrer R., Neronov A., 2013, A&AR, 21, 62
Federrath C., Roman-Duval J., Klessen R. S., Schmidt W., Mac Low M.-M., 2010, A&A, 512, A81
Federrath C., Chabrier G., Schober J., Banerjee R., Klessen R. S., Schleicher D. R. G., 2011a, Phys. Rev. Lett., 107, 114504
Federrath C., Sur S., Schleicher D. R. G., Banerjee R., Klessen R. S., 2011b, ApJ, 731, 62
Federrath C., Schober J., Bovino S., Schleicher D. R. G., 2014, ApJ, 797, L19
Fields B. D., Olive K. A., Yeh T.-H., Young C., 2020, J. Cosmol. Astropart. Phys., 3, 010
Gardner J. P. et al., 2006, Space Sci. Rev., 123, 485
Gerrard I. A., Federrath C., Kuruwita R., 2019, MNRAS, 485, 5532
Girichidis P., Konstandin L., Whitworth A. P., Klessen R. S., 2014, ApJ, 781, 91
Glassgold A. E., Krstić P. S., Schultz D. R., 2005, ApJ, 621, 808
Gray W. J., McKee C. F., Klein R. I., 2018, MNRAS, 473, 2124
Greif T. H., White S. D. M., Klessen R. S., Springel V., 2011, ApJ, 736, 147
Greif T. H., Bromm V., Clark P. C., Glover S. C. O., Smith R. J., Klessen R. S., Yoshida N., Springel V., 2012, MNRAS, 424, 399
Haiman Z., Thoul A. A., Loeb A., 1996, ApJ, 464, 523
Harrison E. R., 1969, Nature, 224, 1089
Harrison E. R., 1970, MNRAS, 147, 279
Haugen N. E., Brandenburg A., Dobler W., 2004, Phys. Rev. E, 70, 016308
Johnson J. L., Greif T. H., Bromm V., 2007, ApJ, 665, 85
Karlsson T., Bromm V., Bland-Hawthorn J., 2013, Rev. Mod. Phys., 85, 809
Kazantsev A. P., 1968, J. Exp. Theor. Phys., 26, 1031
Kitayama T., Yoshida N., Susa H., Umemura M., 2004, ApJ, 613, 631
Koh D., Wise J. H., 2016, MNRAS, 462, 81
Krumholz M. R., Federrath C., 2019, Front. Astron. Space Sci., 6, 7
Kulsrud R. M., 2005, Plasma Physics for Astrophysics. Wiley, New York
Kulsrud R. M., Anderson S. W., 1992, ApJ, 396, 606
Kulsrud R. M., Zweibel E. G., 2008, Rep. Prog. Phys., 71, 046901
Kulsrud R. M., Cen R., Ostriker J. P., Ryu D., 1997, ApJ, 480, 481
Lazarian A., Eyink G. L., Vishniac E. T., Kowal G., 2015, in Lazarian A., de Gouveia Dalpino E. M., Melioli C., eds, Astrophysics and Space Science Library, Vol. 407, Magnetic Fields in Diffuse Media. Springer-Verlag, Berlin. p. 311
Lecoanet D. et al., 2016, MNRAS, 455, 4274
Lesaffre P., Balbus S. A., 2007, MNRAS, 381, 319
Li P. S., Martin D. F., Klein R. I., McKee C. F., 2012, ApJ, 745, 139
Li P. S., McKee C. F., Klein R. I., 2015, MNRAS, 452, 2500
Machida M. N., Doi K., 2013, MNRAS, 435, 3283
Machida M. N., Omukai K., Matsumoto T., Inutsuka S.-I., 2006, ApJ, 647, L1
McKee C. F., 1989, ApJ, 345, 782
McKee C. F., Ostriker E. C., 2007, ARA&A, 45, 565
Madau P., Ferrara A., Rees M. J., 2001, ApJ, 555, 92
Mocz P., Burkhart B., Hernquist L., McKee C. F., Springel V., 2017, ApJ, 838, 40
Moffatt H. K., 1961, J. Fluid Mech., 11, 625
Naoz S., Narayan R., 2013, Phys. Rev. Lett., 111, 051303
Neronov A., Vovk I., 2010, Science, 328, 73
Peters T., Schleicher D. R. G., Smith R. J., Schmidt W., Klessen R. S., 2014, MNRAS, 442, 311
Pinto C., Galli D., 2008, A&A, 484, 1
Pinto C., Galli D., Bacciotti F., 2008, A&A, 484, 1
Pope S. B., 2000, Turbulent Flows. Cambridge Univ. Press, Cambridge, p. 806
Price D. J., 2012a, J. Comput. Phys., 231, 759
Price D. J., 2012b, MNRAS, 420, L33
Pudritz R. E., Silk J., 1989, ApJ, 342, 650
Schekochihin A. A., Cowley S. C., Hammett G. W., Maron J. L., McWilliams J. C., 2002a, New J. Phys., 4, 84
Schekochihin A. A., Boldyrev S. A., Kulsrud R. M., 2002b, ApJ, 567, 828
Schleicher D. R. G., Banerjee R., Sur S., Arshakian T. G., Klessen R. S., Beck R., Spaans M., 2010, A&A, 522, A115
Schober J., Schleicher D., Federrath C., Klessen R., Banerjee R., 2012a, Phys. Rev. E, 85, 026303
Schober J., Schleicher D., Federrath C., Glover S., Klessen R. S., Banerjee R., 2012b, ApJ, 754, 99
Schober J., Schleicher D. R. G., Federrath C., Bovino S., Klessen R. S., 2015, Phys. Rev. E, 92, 023010
Schober J., Rogachevskii I., Brandenburg A., Boyarsky A., Fröhlich J., Ruchayskiy O., Kleeorin N., 2018, ApJ, 858, 124
Sharda P., Federrath C., Krumholz M. R., 2020, preprint (arXiv:2002.11502)
Sokasian A., Yoshida N., Abel T., Hernquist L., Springel V., 2004, MNRAS, 350, 47
Spitzer L., 1968, Diffuse Matter in Space. Princeton Univ. Press, Princeton, NJ
Stacy A., Greif T. H., Bromm V., 2010, MNRAS, 403, 45

Stacy A., Greif T. H., Bromm V., 2012, MNRAS, 422, 290
Stacy A., Bromm V., Lee A. T., 2016, MNRAS, 462, 1307
Subramanian K., 2016, Rep. Prog. Phys., 79, 076901
Sur S., Schleicher D. R. G., Banerjee R., Federrath C., Klessen R. S., 2010, ApJ, 721, L134
Tan J. C., Blackman E. G., 2004, ApJ, 603, 401
Tan J. C., McKee C. F., 2004, ApJ, 603, 383
Taylor A. M., Vovk I., Neronov A., 2011, A&A, 529, A144
Tegmark M., Silk J., Rees M. J., Blanchard A., Abel T., Palla F., 1997, ApJ, 474, 1
Tricco T. S., Price D. J., Federrath C., 2016, MNRAS, 461, 1260
Truelove J. K., Klein R. I., McKee C. F., Holliman J. H., II, Howell L. H., Greenough J. A., 1997, ApJ, 489, L179
Turk M. J., Abel T., O'Shea B., 2009, Science, 325, 601
Turk M. J., Oishi J. S., Abel T., Bryan G. L., 2012, ApJ, 745, 154
Turner M. S., Widrow L. M., 1988, Phys. Rev. D, 37, 2743
Tzeferacos P. et al., 2018, Nat. Commun., 9, 591
Vranjes J., Krstic P. S., 2013, A&A, 554, A22
Wagstaff J. M., Banerjee R., Schleicher D., Sigl G., 2014, Phys. Rev. D, 89, 103001
Whalen D., Abel T., Norman M. L., 2004, ApJ, 610, 14
Xu H., O'Shea B. W., Collins D. C., Norman M. L., Li H., Li S., 2008, ApJ, 688, L57
Xu S., Lazarian A., 2016, ApJ, 833, 215
Xu S., Garain S. K., Balsara D. S., Lazarian A., 2019, ApJ, 872, 62
Yoshida N., Abel T., Hernquist L., Sugiyama N., 2003, ApJ, 592, 645
Yoshida N., Omukai K., Hernquist L., 2008, Science, 321, 669

APPENDIX A: VISCOSITY AND RESISTIVITY OF PRIMORDIAL GAS

A1 Viscosity

For a primordial gas with $n_{\rm He}/n_{\rm H} \lesssim 0.1$, the viscosity is very close to that of atomic hydrogen. A fit to the results of Vranjes & Krstic (2013) for the dynamic viscosity of atomic hydrogen based on the measured cross-section for H–H scattering gives

$$\eta_{\rm visc,HH} = 1.14 \times 10^{-5} T_3^{0.84}\ {\rm kg\ s^{-1}\ m^{-1}}. \tag{A1}$$

They quote (3.95, 5.5, 8.6) $\times\ 10^{-5}$ kg s^{-1} m^{-1} at $T =$ (4400, 6560, 11150) K, whereas the fit gives (3.96, 5.53, 8.64), for excellent agreement. There are no data for $T = 1000$ K, but the cross-section for H–H scattering, $\sigma_{\rm HH}$, continues to rise and $\eta_{\rm visc,\,HH} \propto 1/\sigma_{\rm HH}$ continues to fall as the energy decreases, consistent with the behaviour of equation (A1). In cgs units, the viscosity is 10 times larger. We adopt a helium abundance $n_{\rm He}/n_{\rm H} = 1/12$, a good approximation to the most recent value (1/12.20) from big bang nucleosynthesis combined with observations of the cosmic microwave background (Fields et al. 2020). The mass per H nucleus is then $\mu_{\rm H} = 2.23 \times 10^{-24}$ g, and the kinematic viscosity is

$$\nu \simeq \frac{\eta_{\rm visc,HH}}{\rho} = \frac{\eta_{\rm visc,HH}}{n_{\rm H}\mu_{\rm H}} = 5.11 \times 10^{19}\,\frac{T_3^{0.84}}{n_{\rm H}}\ {\rm cm^2\ s^{-1}}. \tag{A2}$$

A2 Ambipolar resistivity

The ambipolar resistivity (in the terminology of Pinto et al. 2008) is

$$\eta_{\rm AD} = \frac{B^2}{4\pi\rho_{\rm i}\nu_{\rm in}} = \frac{B^2}{4\pi\rho_{\rm i}\rho_{\rm n}\gamma_{\rm AD}}, \tag{A3}$$

where $\rho_{\rm i}$ is the mass density of ions, $\nu_{\rm in}$ is the ion–neutral collision frequency, and the collisional drag coefficient, $\gamma_{\rm AD}$, is defined through

$$\rho_{\rm i}\nu_{\rm in} = \rho_{\rm i}\rho_{\rm n}\gamma_{\rm AD}. \tag{A4}$$

The expression for $\eta_{\rm AD}$ follows from balancing the drag force, $\rho_{\rm i}\nu_{\rm in}v_{\rm d}$, where $v_{\rm d}$ is the relative ion–neutral velocity, with the Lorentz force, $B^2/4\pi\ell_B$, where ℓ_B is the length scale over which the field varies, and then setting $\eta_{\rm AD} \sim \ell_B v_{\rm d}$ (for an actual derivation, see Brandenburg & Zweibel 1994 or Pinto et al. 2008). In our case, there is one dominant ion, H^+, and (prior to molecule formation) two dominant neutrals, H and He. For low ionization, H and He will have the same velocity, so that

$$\rho_{\rm i}\nu_{\rm in} = \Sigma_j n_i n_j \mu_{ij} \langle\sigma v\rangle_{ij} \tag{A5}$$

(Glassgold, Krstić & Schultz 2005), where the sum is over the neutrals and μ_{ij} is the reduced mass. Because the H^+–He collision rate is only about 1/6 of the H^+–H collision rate Pinto & Galli 2008) and the He abundance is low ($x_{\rm He} \equiv n_{\rm He}/n_{\rm H} = 1/12$), H^+–He collisions make a negligible contribution to the ion–neutral collision rate. Under the assumption that the ionization is very small, we then have

$$\nu_{\rm in} = \frac{1}{2} n_{\rm H} \langle\sigma v\rangle_{\rm HH^+}. \tag{A6}$$

The neutral density is $\rho_{\rm n} = (1 + 4x_{\rm He}) n_{\rm H} m_{\rm H}$, so that

$$\gamma_{\rm AD} = \frac{\nu_{\rm in}}{\rho_{\rm n}} = \frac{\langle\sigma v\rangle_{\rm HH^+}}{2(1 + 4x_{\rm He}) m_{\rm H}}. \tag{A7}$$

In the text, we also need the neutral–ion collision frequency, $\nu_{\rm ni}$, which satisfies $\rho_{\rm n}\nu_{\rm ni} = \rho_{\rm i}\nu_{\rm in}$, so that $\nu_{\rm ni} = \rho_{\rm i}\gamma_{\rm AD}$. Glassgold et al. (2005) modified Draine's (1980) determination of the rate coefficient for H–H^+ collisions, obtaining $\langle\sigma v\rangle_{\rm HH^+} = 2.13 \times 10^{-9} v_{\rm rms,5}^{0.75}$ cm^3 s^{-1} for $v_{\rm rms} > 1$ km s^{-1}, which leads to

$$\gamma_{\rm AD} = 6.36 \times 10^{14} \left(\frac{v_{\rm rms,5}^{0.75}}{1 + 4x_{\rm He}}\right)\ {\rm cm^3\ s^{-1}\ g^{-1}}. \tag{A8}$$

For $x_{\rm He} = 0.1$, this agrees with the result of Glassgold et al. (2005); for $x_{\rm He} = 1/12$, this gives $\gamma_{\rm AD} = 4.77 \times 10^{14} v_{\rm rms,5}^{0.75}$ cm^3 s^{-1} g^{-1}.

To express $\gamma_{\rm AD}$ in terms of the temperature, we note that for two species, s and s', with Maxwellian velocity distributions moving at a relative velocity $v_{\rm d}$, we have

$$v_{\rm rms} = \left(v_{\rm d}^2 + \frac{8kT_{ss'}}{\pi\mu_{ss'}}\right)^{1/2}, \tag{A9}$$

where

$$T_{ss'} = \frac{m_{s'}T_s + m_s T_{s'}}{m_s + m_{s'}} \rightarrow T, \tag{A10}$$

$$\mu_{ss'} = \frac{m_s m_{s'}}{m_s + m_{s'}} \rightarrow \frac{1}{2} m_{\rm H} \tag{A11}$$

(e.g. Pinto & Galli 2008) and where the simplified results apply to an H–H^+ plasma.[3] Expressing $v_{\rm rms}$ as

$$v_{\rm rms} = \left(\frac{8kT_{ss'}}{\pi\mu_{ss'}}\right)^{1/2} \phi_{\rm d}^{4/3}, \tag{A12}$$

we have for H–H^+ collisions

$$v_{\rm rms} = 6.48 \times 10^5\, \phi_{\rm d}^{4/3} T_3^{1/2}\ {\rm cm\ s^{-1}}, \tag{A13}$$

$$\phi_{\rm d} = \left[1 + \left(\frac{v_{\rm d,5}}{6.48}\right)^2 \frac{1}{T_3}\right]^{0.375}, \tag{A14}$$

$$\langle\sigma v\rangle_{\rm HH^+} = 8.65 \times 10^{-9} \phi_{\rm d} T_3^{0.375}\ {\rm cm^3\ s^{-1}}, \tag{A15}$$

[3]Note that for $v_{\rm d} = 0$, $v_{\rm rms}$ is actually the mean particle velocity, not the rms velocity, but we follow the notation of Pinto & Galli (2008) here.

$$\gamma_{\rm AD} = 1.94 \times 10^{15}\, \phi_{\rm d} T_3^{0.375}\ {\rm cm^3\ s^{-1}\ g^{-1}}, \tag{A16}$$

$$\nu_{\rm ni} = \rho_{\rm i} \gamma_{\rm AD}, \tag{A17}$$

$$\nu_{\rm ni} = 3.24 \times 10^{-13}\, \phi_{\rm d} x_{\rm i,-4} n_{\rm H} T_3^{0.375}\ {\rm s^{-1}}, \tag{A18}$$

where $\phi_{\rm d}$ is determined from equation (A9), the final two expressions are for $x_{\rm He} = 1/12$, and $x_{\rm i,-4} = (n_{\rm i}/n_{\rm H})/10^{-4}$ is the normalized ionization fraction. Our result for $\gamma_{\rm AD}$ is larger than that of Xu & Lazarian (2016) since we used the value of $\langle \sigma v \rangle$ given by Glassgold et al. (2005) instead of that by Draine, Roberge & Dalgarno (1983); in addition, the value adopted by Xu & Lazarian (2016) appears to be for the case of molecular clouds, for which the dominant ions are heavy molecules such as HCO^+.

Since the magnetic field and therefore the ambipolar resistivity, $\eta_{\rm AD} \propto B^2$, vary by orders of magnitude, it is convenient to express $\eta_{\rm AD}$ in normalized form. Normalizing the Alfvén velocity with respect to the turbulent velocity on large scales, $v_{\rm t}$, and the field relative to the equipartition value at the viscous scale, B_ν (equation 12), we have

$$\eta_{\rm AD} = 3.08 \times 10^{22} \left(\frac{v_{\rm t,5}^2}{\phi_{\rm d} x_{\rm i,-4} n_{\rm H} T_3^{0.375}} \right) \frac{v_{\rm A}^2}{v_{\rm t}^2}\ {\rm cm^2\ s^{-1}}, \tag{A19}$$

$$\eta_{\rm AD} = 3.96 \times 10^{20} \left(\frac{T_3^{0.04} v_{\rm t,5}^{3/2}}{\phi_{\rm d} x_{\rm i,-4} n_{\rm H}^{3/2} r_{\rm pc}^{1/2}} \right) \frac{B^2}{B_\nu^2}\ {\rm cm^2\ s^{-1}}. \tag{A20}$$

Alternatively, in terms of $\beta = 8\pi\rho c_{\rm s}^2/B^2 = 2c_{\rm s}^2/v_{\rm A}^2$, we have

$$\eta_{\rm AD} = \frac{2c_{\rm s}^2}{\beta \rho_{\rm i} \gamma_{\rm AD}} = 4.13 \times 10^{23} \left(\frac{T_3^{0.62}}{\phi_{\rm d} x_{\rm i,-4} n_{\rm H} \beta} \right)\ {\rm cm^2\ s^{-1}}. \tag{A21}$$

A3 Ohmic resistivity

As noted by previous authors (e.g. Kulsrud & Anderson 1992), the Ohmic resistivity is generally negligible compared to the AD resistivity unless the field is very weak: Since the drag due to ion–neutral collisions is much greater than that due to electron–neutral collisions, the Ohmic resistivity is determined by electron–ion and electron–neutral interactions

Pinto et al. 2008),

$$\eta_{\rm O} = \frac{c^2}{4\pi} \left(\frac{m_{\rm e}}{e^2 n_{\rm e}} \right) (\nu_{\rm ei} + \nu_{\rm en}), \tag{A22}$$

where

$$\nu_{ss'} = \left(\frac{m_{s'}}{m_s + m_{s'}} \right) n_{s'} \langle \sigma v \rangle_{ss'} \tag{A23}$$

is the collision rate for momentum transfer between particles of type s and those of type s'. (We follow Pinto et al. 2008 in writing $\eta_{\rm O} = c^2/(4\pi\sigma_{\rm cond})$ for the Ohmic resistivity, where $\sigma_{\rm cond}$ is the electrical conductivity.) Pinto & Galli (2008) give

$$\langle \sigma v \rangle_{\rm eH^+} = \frac{2.30 \times 10^{-3}}{T_3^{3/2}} \left(\frac{\ln \Lambda}{20} \right)\ {\rm cm^3\ s^{-1}}, \tag{A24}$$

$$\langle \sigma v \rangle_{\rm eH} = 1.41 \times 10^{-7} T_3^{0.6} \exp\left(-0.43 T_3^{1/2} \right)\ {\rm cm^3\ s^{-1}}, \tag{A25}$$

where $\ln \Lambda$ is the Coulomb logarithm and where we have assumed that the drift velocity of the electrons relative to the neutrals is much less than 100 km s^{-1} in the second expression. As a result, we have

$$\eta_{\rm O} = \left[\frac{6.5 \times 10^8}{T_3^{3/2}} \left(\frac{\ln \Lambda}{20} \right) + \frac{4.0 \times 10^8 T_3^{0.6}}{x_{\rm i,-4}} \exp\left(-0.43 T_3^{1/2} \right) \right]\ {\rm cm^2\ s^{-1}}, \tag{A26}$$

which is negligible compared to $\eta_{\rm AD}$ for $n_{\rm H}\beta \ll 10^{15}$ cm^{-3}. More specifically, ambipolar diffusion dominates electron–ion Ohmic resistivity and electron–neutral Ohmic resistivity for

$$B > 8.9 \times 10^{-14} \left[\frac{x_{\rm i,-4} \phi_{\rm d}}{T_3^{1.12}} \left(\frac{\ln \Lambda}{20} \right) \right]^{1/2} n_{\rm H}\ {\rm G}, \tag{A27}$$

$$B > 7.0 \times 10^{-14} \phi_{\rm d}^{1/2} T_3^{0.49} \exp\left(-0.22 T_3^{1/2} \right) n_{\rm H}\ {\rm G}, \tag{A28}$$

respectively. Hence, ambipolar diffusion is typically dominant for $B \gtrsim 10^{-13} n_{\rm H}$ G.

APPENDIX B: FREE-FALL COLLAPSE

Gravitational collapse is often described approximately by the collapse of a uniform, pressureless sphere of gas, which has the parametric solution (Spitzer 1968)

$$r = r_0 \cos^2 \psi, \tag{B1}$$

$$\psi + \frac{1}{2} \sin\, 2\psi = \frac{\pi}{2} \left(\frac{t}{t_{\rm ff,0}} \right), \tag{B2}$$

where $t_{\rm ff,0} = (3\pi/32 G\rho_0)^{1/2} = 1.41 \times 10^{15} n_{\rm H,0}^{-1/2}$ s is the initial free-fall time of the gas – i.e. the time at which a cloud beginning at rest with a radius r_0 collapses to a singularity. In cosmology, this is the tophat solution. Girichidis et al. (2014) have shown that it is possible to obtain an accurate approximation for the time as a function of the radius for free-fall collapse; unfortunately, solving this relation for the radius as a function of time does not give an accurate result at late times. Instead, one can show that in a free-fall collapse, gas that is initially static at a radius r_0 is at a radius

$$r = \phi_r r_0 (1 - \tau^2)^{2/3} \tag{B3}$$

at a time t, where $\tau \equiv t/t_{\rm ff,0}$. The factor $\phi_r \to 1$ for $\tau \to 0$ and $\phi_r \to (3\pi/8)^{2/3} = 1.115$ for $\tau \to 1$. The approximation $\phi_r \simeq 1.05$ is accurate to within 6 per cent for all τ between 0 and 1. An approximation that is accurate to within 0.3 per cent for all τ in this range is

$$\phi_r \simeq \left[0.234 + 0.766 \left(1 - \tau^{3/2} \right)^{2/3} \right]^{-0.075}. \tag{B4}$$

The normalized density is

$$\xi \equiv \frac{\rho}{\rho_0} = \left(\frac{r_0}{r} \right)^3 = \frac{1}{\phi_r^3 (1 - \tau^2)^2}. \tag{B5}$$

Taking $\phi_r = (1, 1.05)$ gives an accuracy of (40 per cent, 20 per cent) for the density, respectively; taking $1/\phi_r^3 = (8/3\pi)^2 = 0.72$ is accurate to 10 per cent for $\rho > 100\rho_0$. The time is given by

$$\tau = \left[1 - \left(\frac{\rho_0}{\phi_r^3 \rho} \right)^{1/2} \right]^{1/2} \to 1 - \frac{4}{3\pi} \left(\frac{\rho_0}{\rho} \right)^{1/2}, \tag{B6}$$

where the final step gives an accuracy for $1 - \tau$ that is better than 10 per cent for $\rho > 100\rho_0$.

In minihaloes, dark matter is initially dominant, so we generalize the treatment above to allow for this. In addition, we allow for the

possibility that the collapse occurs at a rate $\phi_{\rm ff}$ less than free fall due to the fact that real collapses are not pressureless. The equation of motion for a shell of gas at radius r inside a collapsing cloud is then

$$\frac{{\rm d}v}{{\rm d}t} = -\frac{1}{\phi_{\rm ff}^2}\left[\frac{GM(r)}{r^2} + \frac{4\pi G\rho_{\rm d} r}{3}\right], \tag{B7}$$

where $M(r)$ is the mass of gas inside r and the numerical factor $\phi_{\rm ff} \geq 1$ in the absence of external compression, since the gas pressure resists collapse. We assume that the density of dark matter, $\rho_{\rm d}$, is spatially constant and remains constant in time; that is, we neglect the adiabatic compression of the dark matter, and we assume that the free-fall time is much less than the age of the Universe. Note that inside the cloud, we have $M(r) \propto r^3$, so that ${\rm d}v/{\rm d}t \propto r$ and the collapse of a constant-density sphere in a constant-density background is homologous, just as in the case with no dark matter. The solution of this equation is

$$v^2 = v_{\rm g}^2\left[\frac{1}{y} - 1 + f_{\rm db}(1-y^2)\right], \tag{B8}$$

where $y \equiv r/r_0$,

$$v_{\rm g} \equiv \frac{1}{\phi_{\rm ff}}\left[\frac{2GM(r_0)}{r_0}\right]^{1/2}, \tag{B9}$$

and

$$f_{\rm db} \equiv \frac{\Omega_{\rm d}}{2\Omega_{\rm b}}, \tag{B10}$$

which is $f_{\rm db} = 3.25$ for the parameters adopted in the text. At late times in the collapse, when $y \ll 1$, we have

$$v^2 \simeq \frac{2GM(r)}{\phi_{\rm ff}^2 r}, \tag{B11}$$

since $M(r) = M(r_0)$. This relation can be used to determine the value of $\phi_{\rm ff}$ in a simulation.

Since the time for the gas to collapse to infinite density in the absence of dark matter is now $\phi_{\rm ff}t_{\rm ff,0}$, we generalize the definition of τ to

$$\tau = \frac{t}{\phi_{\rm ff}t_{\rm ff,0}}. \tag{B12}$$

Note that $t_{\rm ff,0} = (3\pi/32G\rho_0)^{1/2}$ is the initial free-fall time for the gas alone.

In the text, we need the integral of ξ^q over time,

$$I_q(\xi_1,\xi_2) = \frac{1}{\phi_{\rm ff}t_{\rm ff,0}}\int_{t_1}^{t_2}\xi^q\,{\rm d}t = \int_{\tau_1}^{\tau_2}\xi^q\,{\rm d}\tau, \tag{B13}$$

$$I_q(\xi_1,\xi_2) = \frac{2}{3\pi}\int_{\xi_1}^{\xi_2}\frac{\xi^{q-(3/2)}\,{\rm d}\xi}{\left(1-(1/\xi^{1/3})\right)^{1/2}\left[1+(f_{\rm db}/\xi^{1/3})\left(1+(1/\xi^{1/3})\right)\right]^{1/2}}, \tag{B14}$$

where we used ${\rm d}t = r_0\,{\rm d}y/v$, $y = \xi^{-1/3}$, and $r_0/v_{\rm g}\phi_{\rm ff}t_{\rm ff,0} = 2/\pi$. This expression is exact; it is not based on the approximate result for $r(t)$ given above. For $q = 0$, this gives

$$t(\xi) = \phi_{\rm ff}t_{\rm ff,0}I_0(1,\xi) \tag{B15}$$

and therefore $t(r)$ since $r = r_0\xi^{-1/3}$. Note that the effect of dark matter, which is parametrized by the factor $f_{\rm db}$, becomes negligible at small radii (large ξ). Note also that for large ξ, I_q is proportional to $\xi^{q-1/2}$: the range of time integration scales as the free-fall time, $t_{\rm ff} \propto \xi^{-1/2}$.

It is now possible to determine the collapse time of the gas in the presence of static dark matter, $t_{\rm coll}$. For $q < 1/2$, define $I_{q,\infty} = I_q(1,\infty)$. For $q = 0$, numerical evaluation of the integral in equation (B14) gives the collapse time based on the total amount of matter, $t_{\rm coll}$:

$$I_{0,\infty} = \int_0^{t_{\rm coll}}\frac{{\rm d}t}{\phi_{\rm ff}t_{\rm ff,0}} = \frac{t_{\rm coll}}{\phi_{\rm ff}t_{\rm ff,0}} = 0.46 \tag{B16}$$

for $f_{\rm db} = 3.25$. In the absence of dark matter, one can show that $I_{0,\infty} = 1$ as it should: for $f_{\rm db} = 0$, the collapse time is $t_{\rm coll} = \phi_{\rm ff}t_{\rm ff,0}$, as noted earlier.

We now consider the particular case in which the integration extends from the initial density ($\xi_1 = 1$) to a large density ($\xi_2 \gg 1$) for $f_{\rm db} = 3.25$. For $q < 1/2$, we have

$$I_q(1,\xi_2) \simeq I_{q,\infty} - \frac{2}{3\pi\left((1/2)-q\right)}\xi_2^{-((1/2)-q)} \qquad \left(\xi_2^{1/3} \gg 1\right), \tag{B17}$$

where $I_{q,\infty}$ must be evaluated numerically. For example, for $q = -1/2$, $I_{q,\infty} = 0.278$; for $q = 1/6$, $I_{q,\infty} = 0.639$; and for $q = 5/12$, $I_{q,\infty} = 2.43$. The approximation

$$I_q(1,\infty) = I_{q,\infty} \simeq \frac{0.47}{(1-2q)^{0.87}} \tag{B18}$$

is accurate to within 10 per cent for the range $-1/2 < q < 5/12$. For $q \geq 1/2$, $I_q(1,\xi)$ diverges at large ξ.

For $q = 1/2$, an approximation for $I_{1/2}(1,\xi_2)$ that is accurate to within about 1 per cent is

$$\frac{2}{\pi}\ln\left\{1 + \frac{2\left(\xi_2^{1/3}-1\right)^{1/2}}{1+f'_{\rm db}}\left[\left(\xi_2^{1/3}+f'_{\rm db}\right)^{1/2} + \left(\xi_2^{1/3}-1\right)^{1/2}\right]\right\} \tag{B19}$$

with $f'_{\rm db} = f_{\rm db}[2(1+\xi_2^{-1/3})]^{1/2}$. For $\xi_2^{1/3} \gg 1$, $I_{1/2} \rightarrow (2/3\pi)\ln\xi_2$.

For $q > 1/2$, we have

$$I_q(1,\xi_2) \simeq \frac{2}{3\pi\left(q-(1/2)\right)}\left(\xi_2^{q-(1/2)}-1\right) \qquad \left(\xi_2^{1/3} \gg 1\right). \tag{B20}$$

Finally, in order to treat small-scale dynamos in collapsing gas clouds with no dark matter, one needs to know the values of I_q in this case as well. For $q = 1/2$, the value of I_q is given by equation (B19) with $f'_{\rm db} = 0$; for $q > 1/2$, equation (B20) applies as is. For $q < 1/2$, equation (B17) applies with

$$I_{q,\infty} = \frac{2}{3\sqrt{\pi}\left((1/2)-q\right)}\frac{\Gamma\left((5/2)-3q\right)}{\Gamma(2-3q)}. \tag{B21}$$

APPENDIX C: NUMERICAL VISCOSITY AND RESISTIVITY

Here, we estimate the numerical viscosity in both grid-based and SPH codes. We begin by presenting a method of determining the numerical viscosity for subsonic turbulence based on the fact that viscosity suppresses the $k^{-5/3}$ energy spectrum of Kolmogorov turbulence by a factor (Pope 2000)

$$f(k\ell_\nu) \simeq \exp\left(-5.2\left\{\left[(k\ell_\nu)^4 + 0.4^4\right]^{1/4} - 0.4\right\}\right), \tag{C1}$$

where k is the wavenumber, $\ell_\nu = (\nu^3/\epsilon)^{1/4}$ is the viscous scale (equation 3), and $\epsilon = v_\ell^3/\ell$ is the constant energy flux in the turbulence. Pope (2000) showed that this is in good agreement with experimental data and Bauer & Springel (2012) have shown that it accurately describes the turbulent energy spectrum calculated with the AREPO code (with the exception of the bottleneck effect, which is absent from the result of Pope 2000), in both its fixed grid and

moving mesh versions. Numerical viscosity is not exactly equivalent to a physical viscosity. One manifestation of this is that turbulence simulations without a physical viscosity show a larger bottleneck effect than those that solve the Navier–Stokes equations and resolve the dissipation range (Springel, private communication). Another is that the effective Reynolds number in simulations of turbulent mixing is problem dependent (Lecoanet et al. 2016). Nonetheless, as shown by the excellent agreement Bauer & Springel (2012) found between their turbulence simulations and equation (C1), that equation provides a reasonable basis for estimating the effective numerical viscosity.

Equation (C1) predicts that viscosity has a substantial effect on the turbulence when $f = 1/2$, which occurs at $k_{1/2}\ell_\nu = 0.485 \simeq 0.5$. Since the viscosity is $\nu = \ell_\nu^{4/3}\epsilon^{1/3}$, it follows that

$$\nu = 0.40\left(\frac{\epsilon}{k_{1/2}^4}\right)^{1/3} = 0.034\left(\frac{\epsilon L^4}{k_{1/2}'^4}\right)^{1/3}, \tag{C2}$$

where we have also expressed the viscosity in terms of the normalized wavenumber, $k' = kL/2\pi$, which ranges from 1 to $\mathcal{N}_g$ in grid-based simulations and which is often used in reporting the results of simulations. Since Pope's (2000) expression does not include the bottleneck effect, that effect must be eliminated in evaluating $k_{1/2}$.

We validate this approach by comparing with the results of Bauer & Springel (2012). They carried out a simulation with the AREPO code with a sound speed $c_s = 1$, Mach number $\mathcal{M} = 0.3$, and a box size $L = 1$, so that $\epsilon = v_L^3/L = 0.3^3 = 0.027$. The simulation corresponded to $\mathcal{N}_g = 256$ cells in each direction, and the total (physical plus numerical) viscosity was $\nu = 1.5 \times 10^{-4}$. After removing the bottleneck effect apparent in their results, we estimate $k_{1/2} \simeq 140$ from their plot of the velocity power spectrum – i.e. the normalized power spectrum at $k = 140$ is half the value it has at $k = 2\pi$. (In terms of k', their results show that the normalized power spectrum at $k' = 22$ is half the value it has at $k' = 1$.) According to equation (C2), this corresponds to a viscosity $\nu = 1.65 \times 10^{-4}$, in excellent agreement with their value in view of the uncertainty in the estimate of $k_{1/2}$.

C1 Grid-based codes

First consider grid-based codes, which have cells of size $\Delta x = L/\mathcal{N}_g$. The numerical viscosity in the grid-based FLASH code has been evaluated by Benzi et al. (2008) through analysis of the longitudinal structure function, and was found to correspond to $\ell_\nu \simeq 0.6\Delta x$. It follows that the numerical viscosity for grid-based codes is

$$\nu_g = \ell_\nu^{4/3}\epsilon^{1/3} = \frac{\ell_\nu^{4/3} v_L}{L^{1/3}} \simeq 0.5 v_L \Delta x \left(\frac{\Delta x}{L}\right)^{1/3}, \tag{C3}$$

$$\nu_g = 0.5\left(\frac{v_L \Delta x}{\mathcal{N}_g^{1/3}}\right), \tag{C4}$$

where v_L is the velocity on the scale L. More precisely, $v_L = (\epsilon L)^{1/3}$, where ϵ is the specific energy dissipation rate (equation 2); while it is comparable to the rms turbulent velocity, v_t, in a simulation, there is no assurance that the two velocities are equal. Nonetheless, since v_t is generally the only global velocity quoted in simulations, we shall use it in estimating the numerical viscosity.

Although equation (C1) was obtained for incompressible hydrodynamic turbulence, it works for supersonic turbulence and MHD turbulence as well. (However, the results for the viscosity are valid only for subsonic turbulence since they are based on Kolmogorov scaling.) Noting that $\Delta x = L/\mathcal{N}_g$, we have

$$\frac{\ell_\nu}{\Delta x} = \frac{k_{1/2}\ell_\nu}{k_{1/2}\Delta x} \simeq \frac{0.5}{2\pi k_{1/2}'\Delta x/L} = \frac{\mathcal{N}_g}{4\pi k_{1/2}'} \tag{C5}$$

for $k_{1/2} \simeq 0.5/\ell_\nu$. We estimate $k_{1/2}' = 150$ for the Mach 5.5 simulation on a 1024^3 grid by Federrath et al. (2010), which gives $\ell_\nu = 0.54\Delta x$. For the MHD simulation with a sonic Mach number of 10 and an Alfvén Mach number of $\sqrt{5}$ on a 512^3 grid by Li et al. (2012), we estimate $k_{1/2}' = 62$, corresponding to $\ell_\nu = 0.66\Delta x$. In both cases, these results are quite close to the value found by Benzi et al. (2008). The corresponding result for AREPO is $\ell_\nu = 0.9\Delta x$, which is larger than the other values because it included a physical viscosity. For the value we adopt, $\ell_\nu = 0.6\Delta x$ (Benzi et al. 2008), we have $k_{1/2}' = \mathcal{N}_g/(2.4\pi) = \mathcal{N}_g/7.5$.

The Reynolds number based on equation (C4) is

$$Re = \frac{L v_L}{\nu_g} = \frac{L v_L}{0.5 v_L \Delta x/\mathcal{N}_g^{1/3}} = 2\mathcal{N}_g^{4/3}. \tag{C6}$$

This result can also be derived directly from equation (4):

$$Re = \left(\frac{L}{\ell_\nu}\right)^{4/3} = \left(\frac{\mathcal{N}_g}{\ell_\nu/\Delta x}\right)^{4/3}, \tag{C7}$$

which is $1.98\mathcal{N}_g^{4/3}$ for $\ell_\nu = 0.6\Delta x$. By contrast, Federrath et al. (2011b) suggested $\ell_\nu = 2\Delta x$, which leads to $Re = 0.4\mathcal{N}_g^{4/3}$. We note that their value for ℓ_ν is much larger than the value we inferred from Federrath et al. (2010), which is in good agreement with the value obtained by Benzi et al. (2008).

As a further comparison with results in the literature, we evaluate the wavenumber at which numerical dissipation begins to affect the results. To make this quantitative, let $k_{1-\delta}$ be the wavenumber at which $f = 1 - \delta$. Equation (C1) implies that

$$k_{1-\delta}\ell_\nu \simeq 0.47\delta^{1/4} \tag{C8}$$

to within about 3 per cent for $\delta < 0.1$. Noting that $k\ell_\nu = (2\pi k'/L)0.6\Delta x$, we find $k_{1-\delta}' = 0.125\delta^{1/4}\mathcal{N}_g$. Federrath et al. (2010) concluded that numerical dissipation begins to affect their results at $k' \simeq 40$ in their 1024^3 simulations. Inspection of their results shows that δ is much less than 0.1 at $k' = 40$. Equation (C8) implies $k_{1-\delta}' = 40$ for $\delta = 0.01$, with only a weak dependence on the value of δ, consistent with their result.

Finally, we note that for an AMR code like ORION, the cell size for problems involving self-gravity is generally set by the requirement that the Jeans length, $\lambda_J = (\pi c_s^2/G\rho)^{1/2}$, be well resolved (Truelove et al. 1997). Cells are refined to higher levels if their density exceeds the Truelove–Jeans density, ρ_{TJ}, which is set by the condition

$$\Delta x = J_{max}\lambda_J(\rho_{TJ}), \tag{C9}$$

where $J_{max} \leq 1/4$ is provided by the user, so that

$$\rho_{TJ} = \frac{\pi J_{max}^2 c_s^2}{G\Delta x^2}. \tag{C10}$$

For cases in which the outer scale of the turbulence is set by self-gravity and the Mach number is of order unity, Federrath et al. (2011b) found that a resolution of 32 zones per Jeans length, $J_{max} = 1/32$, is sufficient to see amplification by a turbulent dynamo, whereas a resolution of 16 cells per Jeans length is not. Using a somewhat more dissipative code, Turk et al. (2012) found that a resolution of 64 cells per Jeans length was required. In order to express Δx in terms of the local density, we have

$$\Delta x = J_{max}\lambda_J(\rho)\left(\frac{\rho}{\rho_{TJ}}\right)^{1/2}. \tag{C11}$$

At a given level of refinement, the density will range up to $\rho_{\rm TJ}$. The maximum value of $\Delta x(\rho)$, which corresponds to a conservative estimate for the viscosity, occurs for $\rho = \rho_{\rm TJ}$. Normalizing $J_{\rm max}$ to 1/64 then gives

$$\nu_{\rm g} = 1.69 \times 10^{24} \left(\frac{J_{\rm max}}{1/64}\right)^{4/3} \frac{v_{\rm t,5}}{L_{\rm pc}^{1/3}} \left(\frac{T_3}{n_{\rm H}}\right)^{2/3} {\rm cm}^2\,{\rm s}^{-1}, \quad \text{(C12)}$$

where $v_{\rm t,5}$ is the turbulent velocity in km s^{-1}. This is much larger than the atomic viscosity in equation (A2). For AMR codes, this equation should be used only if there is at least one level of refinement, so that equation (C11) with $\rho = \rho_{\rm TJ}$ can be used to set Δx; otherwise, equation (C4) should be used.

If the outer scale of the turbulence is set by the Jeans length ($L = \lambda_{\rm J}$), as argued by Federrath et al. (2011b) for the case of gravitational collapse, the Reynolds number is

$$Re = 2\left(\frac{\lambda_{\rm J}}{\Delta x}\right)^{4/3} = 512\left(\frac{1/64}{J_{\rm max}}\right)^{4/3} \quad \text{(C13)}$$

from equation (C6), and the viscosity is given by

$$\nu_{\rm g} = 2.32 \times 10^{23} v_{\rm t,5} \left(\frac{J_{\rm max}}{1/64}\right)^{4/3} \left(\frac{T_3}{n_{\rm H}}\right)^{1/2} {\rm cm}^2\,{\rm s}^{-1} \quad \text{(C14)}$$

from equation (C12). If the parameters on the right-hand side of this equation are of order unity, this is more than 1000 times larger than the atomic viscosity; the discrepancy between simulation and reality grows as the density increases.

C2 SPH codes

We now turn our attention to SPH codes. In SPH codes, the viscosity is determined by the artificial viscosity that is added to the code. The standard SPH artificial viscosity corresponds to a Navier–Stokes viscosity (Price 2012a, b)

$$\nu_{\rm sph} = 0.1\,\alpha_{\rm sph}\,c_{\rm s} h_{\rm sm} \quad \text{(C15)}$$

for subsonic flows, where $\alpha_{\rm sph}$ is the SPH artificial viscosity parameter and the smoothing length is given in terms of the particle mass, $m_{\rm sph}$, as

$$h_{\rm sm} = h_{\rm f}(m_{\rm sph}/\rho)^{1/3}. \quad \text{(C16)}$$

Here, $h_{\rm f}$ depends on the number of neighbour particles in a kernel, $\mathcal{N}_{\rm ngb}$,

$$h_{\rm f} = \left(\frac{3\mathcal{N}_{\rm ngb}}{4\pi}\right)^{1/3} \frac{1}{R_{\rm kernel}}, \quad \text{(C17)}$$

where the kernel truncation radius is $R_{\rm kernel} h_{\rm sm}$. Price (2012b) adopted $R_{\rm kernel} = 2$ and $\mathcal{N}_{\rm ngb} \simeq 58$ so that $h_{\rm f} = 1.2$, whereas Stacy et al. (in preparation) adopted $R_{\rm kernel} = 1$ and $\mathcal{N}_{\rm ngb} = 200$ so that $h_{\rm f} = 3.63$. The parameter $\alpha_{\rm sph}$ can be variable and is often set equal to 0.1 far from shocks, giving $\nu_{\rm sph} = 0.01 c_{\rm s} h_{\rm sm}$. However, Bauer & Springel (2012) have argued that this value of $\nu_{\rm sph}$ is too low by a factor of 6. We can resolve this issue by obtaining the value of $\alpha_{\rm sph}$ from equation (C2),

$$\alpha_{\rm sph} = 4.0\left(\frac{\epsilon^{1/3}}{c_{\rm s} h_{\rm sm} k_{1/2}^{4/3}}\right). \quad \text{(C18)}$$

We estimate $k_{1/2} \simeq 75$ for Price's (2012b) 256^3 simulation of $\mathcal{M} = 0.3$ turbulence. He adopted $L = c_{\rm s} = 1$ so that $\epsilon^{1/3} = \mathcal{M} = 0.3$, and the average smoothing length was $h_{\rm sm} = 1.2/256$. Altogether, this gives $\alpha_{\rm sph} = 0.8$, slightly larger than the value 0.6 favoured by Bauer & Springel (2012), but considerably larger than 0.1. Since our estimate is approximate, we shall adopt the value of Bauer & Springel (2012),

$$\nu_{\rm sph} = 0.06\,c_{\rm s} h_{\rm sm}. \quad \text{(C19)}$$

Note that equation (C19) for the SPH viscosity varies linearly with the smoothing length, whereas equation (C6) shows that the grid viscosity varies as $\Delta x^{4/3}$. Equation (C16) then gives

$$\nu_{\rm sph} = 1.50 \times 10^{23} \left(\frac{h_{\rm f} m_{\rm sph}'^{1/3} T_3^{1/2}}{n_{\rm H}^{1/3}}\right) {\rm cm}^2\,{\rm s}^{-1}, \quad \text{(C20)}$$

where $m'_{\rm sph} = m_{\rm sph}/(1\,M_\odot)$. Just as in the case of grid-based viscosity, the numerical viscosity for SPH exceeds the atomic viscosity by more than a factor of 1000 if the parameters on the right-hand side are of order unity, and the discrepancy grows as the density increases. The adiabatic index of the gas varies from $\gamma \simeq 5/3$ for gas in the Hubble flow and gas falling into a dark matter potential well to $\gamma \simeq 1$ for gas in the protostellar core; here, we have set $\gamma = 1$ in our estimate of the SPH viscosity.

For constant density, equation (C19) gives the Reynolds number for SPH,

$$Re = 17\mathcal{M}\left(\frac{L}{h_{\rm sm}}\right) = 17\mathcal{M}\left(\frac{\mathcal{N}_{\rm g,sph}}{h_{\rm f}}\right), \quad \text{(C21)}$$

where $\mathcal{N}_{\rm g,sph} = (\rho L^3/m_{\rm sph})^{1/3}$ is the SPH equivalent to the number of grid cells. The scaling of Re with $\mathcal{M}$ for SPH codes gives them an advantage at high Mach numbers (Price 2012b). The fact that Re scales as $\mathcal{N}_{\rm g}^{4/3}$ for grid-based codes but only as $\mathcal{N}_{\rm g,sph}$ for SPH codes means that grid-based codes become superior to SPH codes at high resolution (Springel 2019, private communication). For the case in which $\mathcal{N}_{\rm g} = \mathcal{N}_{\rm g,sph}$, the resolution of the grid code must exceed $600\mathcal{M}^3$ in order for this advantage to kick in, however.

C3 Numerical resistivity

The numerical resistivity can be inferred from the values of the numerical viscosity above and of the numerical Prandtl number, $P_{\rm m} = \nu/\eta$. Lesaffre & Balbus (2007) found that the numerical Prandtl number for grid-based codes was between 1 and 2, depending on wavenumber. In their simulations of turbulent amplification of magnetic fields, Federrath et al. (2011a) inferred that their results were consistent with this conclusion. Subsequently, Federrath et al. (2011b) studied magnetic field amplification in a gravitationally collapsing cloud. They showed that the Jeans length corresponds to the effective outer scale of the turbulence in such a cloud and that the critical magnetic Reynolds number for dynamo action, $R_{\rm m,cr}$, occurred between 16 and 32 cells per Jeans length. More generally, Haugen et al. (2004) found $R_{\rm m,cr} = 2\pi \times 35 P_{\rm m}^{-1/2}$ for $0.1 \lesssim P_{\rm m} \lesssim 3$. (They defined the magnetic Reynolds number as $R_{\rm m,H} = v/(k_{\rm f}\eta) = vL/(2\pi\eta)$, where $k_{\rm f}$ is the wavenumber at which the turbulence is forced; this is smaller than the value adopted here by a factor of 2π.) Since $Re = R_{\rm m}/P_{\rm m}$, we have $Re_{\rm cr} = 2\mathcal{N}_{\rm g,cr}^{4/3} = 220/P_{\rm m}^{3/2}$. For $\mathcal{N}_{\rm g,cr}$ between 16 and 32, this implies that $P_{\rm m}$ is between 1 and 2, just as Lesaffre & Balbus (2007) found. We shall therefore adopt $P_{\rm m} \simeq 1.4$ for grid-based codes. Tricco et al. (2016) found the magnetic Prandtl number in SPH codes is about 1.2 in the dynamo amplification phase and somewhat less than unity in equipartition; $P_{\rm m}$ also decreases somewhat with resolution. For simplicity, in our analysis we shall adopt $P_{\rm m} = 1.4$ for SPH codes as well as for grid-based codes.

This paper has been typeset from a TEX/LATEX file prepared by the author.